# Dynamic reconfiguration of visuomotor-related functional connectivity networks

Andrea Brovelli, Jean-Michel Badier, Francesca Bonini, Fabrice Bartolomei, Olivier Coulon, Guillaume Auzias

JNeurosci
THE JOURNAL OF NEUROSCIENCE

***Research Articles: Behavioral/Cognitive***

# Dynamic reconfiguration of visuomotor-related functional connectivity networks

**Andrea Brovelli[1], Jean-Michel Badier[2,3], Francesca Bonini[2,3], Fabrice Bartolomei[2,3], Olivier Coulon[1,4,*] and Guillaume Auzias[1,4,*]**

[1]*Institut de Neurosciences de la Timone UMR 7289, Aix Marseille Université, CNRS, 13385, Marseille, France*
[2]*Aix Marseille Université, INS UMR_S 1106, 13005, Marseille, France*
[3]*Inserm, UMR_S 1106, 13005, Marseille, France*
[4]*Aix-Marseille Université, CNRS, LSIS UMR 7296, Marseille, France*

DOI: 10.1523/JNEUROSCI.1672-16.2016

Received: 17 May 2016

Revised: 3 November 2016

Accepted: 12 November 2016

Published: 15 December 2016

**Author contributions:** A.B. designed research; A.B., B.J.-M., and F. Bonini performed research; A.B., F. Bartolomei, O.C., and G.A. contributed unpublished reagents/analytic tools; A.B. analyzed data; A.B., O.C., and G.A. wrote the paper.

*equal contribution

We are extremely thankful to Faical Isbaine and Sophie Chen for helping in the MEG experiments, and to Patrick Marquis and Catherine Liegeois-Chauvel for SEEG experiments. This work was partly supported by Projets exploratoires pluridisciplinaires (PEPS) from the CNRS/Inserm/Inria “Bio-math-Info” entitled “Computational and neurophysiological bases of goal-directed and habit learning”. This work was performed on a MEG platform member of France Life Imaging network (grant ANR-11-INBS-0006).

Corresponding author: Andrea Brovelli, andrea.brovelli@univ-amu.fr, Institut de Neurosciences de la Timone (INT), UMR 7289 CNRS, Aix Marseille University, Campus de Santé Timone, 27 Bd. Jean Moulin, 13385 Marseille, France, Tel.: 0033 4 91 16 43 99, Fax: 0033 4 91 16 44 98

**Cite as:** J. Neurosci 2016; 10.1523/JNEUROSCI.1672-16.2016

# Dynamic reconfiguration of visuomotor-related functional connectivity networks

Andrea Brovelli[1], Jean-Michel Badier[2, 3], Francesca Bonini[2, 3], Fabrice Bartolomei[2,3], Olivier Coulon* [1, 4], Guillaume Auzias* [1, 4]

[1] *Institut de Neurosciences de la Timone UMR 7289, Aix Marseille Université, CNRS, 13385, Marseille, France*
[2] *Aix Marseille Université, INS UMR_S 1106, 13005, Marseille, France*
[3] *Inserm, UMR_S 1106, 13005, Marseille, France*
[4] *Aix-Marseille Université, CNRS, LSIS UMR 7296, Marseille, France*

*equal contribution

Corresponding author:

Andrea Brovelli
andrea.brovelli@univ-amu.fr
Institut de Neurosciences de la Timone (INT),
UMR 7289 CNRS, Aix Marseille University,
Campus de Santé Timone,
27 Bd. Jean Moulin,
13385 Marseille,
France
Tel.: 0033 4 91 16 43 99
Fax: 0033 4 91 16 44 98

Manuscript details:
Number of pages: 34
Number of figures: 8
Number of tables: 2
Number of words: 240 (abstract), 426 (introduction), 1650 (discussion)

Abbreviations

MEG: magnetoencephalography
EEG: electroencephalography

Keywords

High-gamma activity; functional connectivity dynamics; MEG; SEEG; executive functions; dynamic reconfiguration

Acknowledgements

We are extremely thankful to Faical Isbaine and Sophie Chen for helping in the MEG experiments, and to Patrick Marquis and Catherine Liegeois-Chauvel for SEEG experiments. This work was partly supported by Projets exploratoires pluridisciplinaires (PEPS) from the CNRS/Inserm/Inria “Bio-math-Info” entitled “Computational and neurophysiological bases of goal-directed and habit learning”. This work was performed on a MEG platform member of France Life Imaging network (grant ANR-11-INBS-0006).

## ABSTRACT

Cognitive functions arise from the coordination of large-scale brain networks. Yet, the principles governing interareal functional connectivity dynamics (FCD) remain elusive. Here, we test the hypothesis that human executive functions arise from the dynamic interplay of multiple networks. To do so, we investigated FCD mediating a key executing function, known as arbitrary visuomotor mapping, using brain connectivity analyses of high-gamma activity recorded using magnetoencephalography and intracranial electroencephalography. Visuomotor mapping was found to arise from the dynamic interplay of three partly-overlapping cortico-cortical and cortico-subcortical FC networks. First, visual and parietal regions coordinated with sensorimotor and premotor areas. Second, the dorsal fronto-parietal circuit together with the sensorimotor and associative fronto-striatal networks took the lead. Finally, cortico-cortical interhemispheric coordination among bilateral sensorimotor regions coupled with the left fronto-parietal network and visual areas. We suggest that these networks reflect the processing of visual information, the emergence of visuomotor plans and the processing of somatosensory reafference or action's outcomes, respectively. We thus demonstrated that visuomotor integration resides in the dynamic reconfiguration of multiple cortico-cortical and cortico-subcortical FC networks. More generally, we showed that visuomotor-related FC is non-stationary, and displays switching dynamics and areal flexibility over time scales relevant for task performance. In addition, visuomotor-related FC is characterized by sparse connectivity with density less than 10%. To conclude, our results elucidate the relation between dynamic network reconfiguration and executive functions over short time scales, and provide a candidate entry point towards a better understanding of cognitive architectures.

## SIGNIFICANCE STATEMENT

Executive functions are supported by the dynamic coordination of neural activity over large-scale networks. The properties of large-scale brain coordination processes, however, remain unclear. Using tools combining magnetoencephalography and intracranial electroencephalography with brain connectivity analyses, we provide evidence that visuomotor behaviors, a hallmark of executive functions, are mediated by the interplay of multiple and spatially overlapping sub-networks. These sub-networks span visuomotor-related areas, whose cortico-cortical and cortico-subcortical interactions rapidly evolve and reconfigure over time-scales relevant for behavior. Visuomotor-related Functional Connectivity Dynamics (FCD) is characterized by sparse connections, non-stationarity, switching dynamics and areal flexibility. We suggest that these properties represent key aspects of large-scale functional networks and cognitive architectures.

# INTRODUCTION

The dynamic coordination of neural activity over large-scale networks is thought to support cognitive functions (Varela et al., 1999; von der Malsburg et al., 2010; Bressler and Menon, 2010). Growing evidence from fMRI has shown that spontaneous and task-related activity is composed of multiple and spatially overlapping sub-networks that dynamically evolve over tens of seconds to minutes (Hutchinson et al., 2013; Yeo et al., 2013; Allen et al., 2014; Calhoun et al., 2014; Cole et al., 2014; Zalenski et al., 2014; Hansen et al., 2015). Indeed, dynamic network reconfiguration has been suggested to represent a fundamental neurophysiological process supporting executive function (Bassett et al., 2011; Braun et al., 2015).

A hallmark of executive function is the ability to rapidly associate arbitrary actions to visual inputs and internal goals. This ability, known as arbitrary visuomotor mapping, recruits a large-scale network comprising the sensorimotor and frontoparietal circuits, in addition to medial prefrontal areas and basal ganglia (Wise et al., 1996; Murray et al., 2000; Passingham et al., 2000; Wise and Murray, 2000; Hadj-Bouziane et al., 2003; Petrides, 2005). In the current study, the goal was to investigate whether visuomotor mapping results from the dynamic interplay of multiple sub-networks. More precisely, we tested the hypothesis that multiple sub-networks reconfigure in a dynamic fashion over time scales relevant for executive behaviors.

To do so, we exploited the high-gamma activity (ranging from approximately 60 to 150Hz), which reflects population-level local neural activity (Ray et al., 2008; Ray and Maunsell, 2011). In humans, power modulations in the high-gamma range are commonly recorded using magnetoencephalography (MEG) and intracranial electroencephalography to map task-related brain regions (Brovelli et al., 2005; Crone et al., 2006; Vidal et al., 2006; Ball et al., 2008; Jerbi et al., 2009; Darvas et al., 2010; Lachaux et al., 2012; Cheyne and Ferrari, 2013; Ko et al., 2013). Additionally, high-gamma power modulations can be used to characterize functional connectivity (FC) among brain regions supporting executive functions (Brovelli et al., 2015).

Here, we predicted visuomotor mapping to reflect an initial activation of visual circuits mediating the processing of sensory input, followed by fronto-parietal and

123 motor networks for visuomotor integration and motor planning. We tested these
124 hypotheses in a group of healthy participants during MEG recordings by combining
125 FC analysis of atlas-based HGA with methods from network science and graph
126 theory. In particular, we investigated the presence of multiple visuomotor-related
127 spatiotemporal patterns through the analysis of functional connectivity dynamics
128 (FCD). Intracranial assessment of HGA activations from MEG was also performed in
129 three epileptic patients performing the same task during stereo-
130 electroencephalographic (SEEG) recordings.

# MATERIALS & METHODS

## Experimental procedure and data acquisition

### Experimental conditions and behavioral tasks

Eleven healthy participants and three epileptic patients accepted to take part in our study. Healthy participants were right handed and the average age was approximately 23 years (the standard deviation was 3.8 years), 4 were females and 7 males. All gave written informed consent according to established institutional guidelines and local ethics committee, and received monetary compensation (€ 50). Three patients (one right-handed female aged of 29, two right-handed males aged of 29 and 43) undergoing presurgical evaluation of drug-resistant epilepsy (Epilepsy Unit, La Timone Hospital, Marseille, France) participated in this study. They all gave their informed consent prior to their participation. The SEEG study was approved by the Institutional Review Board of the French Institute of Health. Healthy participants and patients performed the same behavioral task. We asked participants to perform an associative visuomotor mapping task, where the relation between visual stimulus and motor response is arbitrary and deterministic (Wise and Murray, 2000; Brovelli et al., 2015). As shown in Figure 1A, the task required participants to perform a finger movement associated to a digit number: digit “1” instructed the execution of the thumb, “2” for the index finger, “3” for the middle finger and so on. Maximal reaction time was 1s. After a fixed delay of 1 second following the disappearance of the digit number, an outcome image was presented for 1 s and informed the subject whether the response was correct, incorrect, or too late (if the reaction time exceeded 1 s). Incorrect and late trials were excluded from the analysis, because they were either absent or very rare (i.e., maximum 2 late trials per session). The next trial started after a variable delay ranging from 2 to 3 s (randomly drawn from a uniform distribution) with the presentation of another visual stimulus. Each participant performed two sessions of 60 trials each (total of 120 trials). Each session included three digits randomly presented in blocks of three trials. The average reaction time was 0.504s ± 0.004s (mean ± s.e.m.).

### Anatomical, functional and behavioral data acquisition in healthy participants

Anatomical MRI images were acquired for healthy participant using a 3-T whole-body imager equipped with a circular polarized head coil. High-resolution

structural T1-weighted anatomical image (inversion-recovery sequence, 1×0.75×1.22 mm) parallel to the anterior commissure-posterior commissure plane, covering the whole brain, were acquired. Magnetoencephalographic (MEG) recordings were performed using a 248 magnetometers system (4D Neuroimaging magnes 3600). Visual stimuli were projected using a video projection and motor responses were acquired using a LUMItouch® optical response keypad with five keys. Presentation® software was used for stimulus delivery and experimental control during MEG acquisition. Reaction times were computed as the time difference between stimulus onset and motor response. Sampling rate was 2034.5 Hz. Location of the participant's head with respect to the MEG sensors was recorded both at the beginning and end of each session to potentially exclude sessions and/or participants with large head movements. For each session and participant, we computed the displacement between the beginning and end of a session. A supine position was chosen to minimize head movements. This cut-off was decided by considering the spatial distance between sources (5mm), as described in the following sections. None of the participants moved more than 3 mm during all sessions. Thus, all participants were considered for further analysis.

Anatomical, functional and behavioral data acquisition in epileptic patients

The surgical treatment of drug-resistant epilepsy may require direct intracerebral recording of cortical activity IEEG in multiple brain areas in order to localize the epileptic tissue to be removed. Before SEEG all patients had high resolution MRI, performed with a 3T Siemens Magnetom scanner (Siemens AG, Erlangen, Germany) including a three-dimensional T1-weighted acquisition. Intracerebral multiple contacts electrodes (10 to 15 contacts, length: 2 mm, diameter: 0.8 mm, 1.5 mm apart) were implanted using a stereotactic method (Talairach et al, 1992). A post-operative computerized tomography (CT) scan without contrast was used to verify the absence of bleeding and the location of each recording lead. During this pre-surgical evaluation period, we asked patients to participate in our behavioral protocol at the Timone Hospital. They were seated in a Faraday cage and stimuli were presented on a display monitor at 70 cm to patient’s eyes with an angular size of 1.26°. Presentation® software was used for stimulus delivery and experimental control during SEEG acquisition. Motor responses were acquired using a 5-button response pad. SEEG signals were acquired on referential montage with a

sampling frequency of 1000 Hz and an acquisition band-pass filter between 0.1 and 200Hz.

## Brain parcellation

In order to map brain activations and Functional Connectivity (FC) patterns to specific anatomical brain networks, single-subject brain parcellation can be created from macro-anatomical information, such as primary and secondary sulci, using either volume-based (Lancaster et al., 2000; Tzourio-Mazoyer et al., 2002) or surface-based (Fischl et al., 1999; Van Essen and Drury, 1997; Desikan et al., 2006) algorithms. Recent developments now allow single-subject cortical parcellation complying with a model of anatomo-functional gradients in the rostro-caudal and dorso-ventral directions (Auzias et al., 2013) optimized for functional mapping using HGA (Auzias et al., 2016). Such approach allows group-level analyses and comparison between individual patients and healthy participants in control group. To do so, we created a whole-brain parcellation including cortical (Figure 1B) and subcortical (Figure 1C) regions based on macro-anatomical information. The identification of the cortical regions requires several processing steps. After denoising using a non-local means approach (Coupé et al., 2008), T1-weighted MR-images were segmented using the FreeSurfer "recon-all" pipeline (http://freesurfer.net). Grey and white matter segmentations of each hemisphere were imported into the BrainVisa software and processed using the Morphologist pipeline procedure (http://brainvisa.info). White matter and pial surfaces were reconstructed and triangulated, and all sulci were detected and labelled automatically (Mangin et al., 2004; Perrot et al., 2011). A parameterization of each hemisphere white matter mesh was performed using the Cortical Surface toolbox (http://www.meca-brain.org/softwares/). It resulted in a 2D orthogonal system defined on the white matter mesh, constrained by a set of primary and secondary sulci (Auzias et al., 2013). This parameterization naturally leads to a complete parcellation of the cortical surface, the *MarsAtlas* model (Auzias et al., 2016).

*MarsAtlas* complies with the dorsoventral and rostrocaudal trends of cortical organization (Régis et al., 2005; Pandya and Yeterian, 1985) and provides a good level of both functional segregation and inter-subject matching for functional analysis using single-trial MEG high-gamma activity (Auzias et al., 2016). The resulting

cortical surface parcellation was then propagated to the volume-based grey matter segmentation, using a front propagation from the surface through the volumetric cortex segmentation (Cachia et al., 2003), hence producing a volume-based parcellation of the entire cortex. The parcels corresponding to the subcortical structures were extracted using Freesurfer (Fischl et al, 2002). The subcortical structures included in the brain parcellation were the caudate nucleus, putamen, nucleus accumbens, globus pallidus, thalamus, amygdala and hippocampus. The whole-brain parcellation therefore comprised 96 areas (41 cortical and 7 subcortical areas per hemisphere) (Figure 1). All these processing steps can be performed using the BrainVisa neuroimaging platform (http://brainvisa.info/web/index.html). *MarsAtlas* is included in the cortical surface toolbox.

## Single-trial high-gamma activity (HGA) in *MarsAtlas*

Preprocessing and spectral analysis of MEG and SEEG signals

The preprocessing and spectral analyses steps for MEG and SEEG signals were identical. Concerning SEEG signals, electrode's contacts owning to the epileptogenic zone were excluded from the analysis. SEEG contacts outside the epileptogenic zone were chosen for analysis. In addition, epochs with signs of epileptic activity were removed. MEG and SEEG signals were first down-sampled to 1 kHz, low-pass filtered to 250 Hz and then segmented into epochs aligned on finger movement (i.e., button press). Epoch segmentation was also performed on stimulus onset and the data from -0.5 and -0.1 s prior to stimulus presentation was taken as baseline activity for the calculation of the single-trial high-gamma activity (HGA). Artefact rejection was performed semi-automatically and by visual inspection. For each movement-aligned epoch and channel, the signal variance and z-value were computed over time and taken as relevant metrics for the identification of artefact epochs. All trials with a variance greater than 1.5*10-24 across channels were excluded from further search of artefacts. Metrics such as the z-score, absolute z-score, and range between the minimum and maximum values were also inspected to detect artefacts. Channels and trials displaying outliers were removed. Two MEG sensors were excluded from the analysis for all subjects.

Spectral density estimation was performed using multi-taper method based on discrete prolate spheroidal (slepian) sequences (Percival and Walden, 1993; Mitra

and Pesaran, 1999). To extract high-gamma activity from 60 to 120, MEG time series were multiplied by *k* orthogonal tapers (*k* = 8) (0.15s in duration and 60Hz of frequency resolution, each stepped every 0.005s), centered at 90Hz and Fourier-transformed. Complex-valued estimates of spectral measures $X^n_{sensor}(t,k)$, including cross-spectral density matrices, were computed at the sensor level for each trial *n*, time *t* and taper *k*.

MEG source analysis and high-gamma activity

Source analysis requires a physical forward model or leadfield, which describes the electromagnetic relation between sources and MEG sensors. The leadfield combines the geometrical relation of sources (dipoles) and sensors with a model of the conductive medium (i.e., the headmodel). For each participant, we generated a headmodel using a single-shell model constructed from the segmentation of the cortical tissue obtained from individual MRI scans as described in section 3.2 (Nolte, 2003). Leadfields were not normalized. Sources were placed in the single-subject volumetric parcellation regions. For each region, we computed the number of sources *nSP* as the ratio of the volume and the volume of a sphere of radius equal to 3 mm. The k-means algorithm (Tou & Gonzalez, 1974) was then used to partition the 3D coordinates of the voxels within a given volumetric region into *nS* clusters. The sources were placed at the center of each partition for each brain region. The headmodel, source locations and the information about MEG sensor position for both models were combined to derive single-participant leadfields. The orientation of cortical sources was set perpendicular to the cortical surface, whereas the orientation for subcortical sources was left unconstrained.

We used adaptive linear spatial filtering (Veen et al., 1997) to estimate the power at the source level. In particular, we employed the Dynamical Imaging of Coherent Sources (DICS) method, a beamforming algorithm for the tomographic mapping in the frequency domain (Gross et al., 2001), which is a well suited for the study of neural oscillatory responses based on single-trial source estimates of band-limited MEG signals (for a series of review see, Hansen et al., 2010). At each source location, DICS employs a spatial filter that passes activity from this location with unit gain while maximally suppressing any other activity. The spatial filters were computed on all trials for each time point and session, and then applied to single-trial MEG data. DICS allows the estimate of complex-value spectral measures at the

source level, $X^n_{source}(t,k) = A(t)X^n_{sensor}(t,k)$, where $A(t)$ is the spatial filter that transforms the data from the sensor to source level and $X^n_{sensor}(t,k)$ is the complex-valued estimates of spectral measures, including cross-spectral density matrices, computed at the sensor level for each trial *n*, time *t* and taper *k* (for a detailed description of a similar approach see (Hipp et al., 2011)). The single-trial high-gamma power at each source location was estimated by multiplying the complex spectral estimates with their complex conjugate, and averaged over tapers *k*, $P^n_{source}(t) = \left\langle X^n_{source}(t,k)X^n_{source}(t,k)^* \right\rangle_k$, where angle brackets refer to the average across tapers and * to the complex conjugate. Single-trial power estimates aligned on movement and stimulus onset were log-transformed to make the data approximate Gaussian and low-pass filtered at 50Hz to reduce noise. Single-trial mean power and standard deviation in a time window from -0.5 and -0.1 s prior to stimulus onset was computed for each source and trial, and used to z-transform single-trial movement-locked power time courses. Similarly, single-trial stimulus-locked power time courses were log-transformed and z-scored with respect to baseline period, so to produce HGAs for the prestimulus period from -1.6 to -0.1 s with respect to stimulation for subsequent functional connectivity analysis. Finally, single-trial HGA for each brain region of *MarsAtlas* was computed as the mean z-transformed power values averaged across all sources within the same region.

SEEG localization and high-gamma activity

Electrodes were localized using the CTMR toolbox (Hermes et al., 2010). Briefly, post-implant CT scans were coregistered and re-sliced to the MRI coordinate scans of each subject using SPM12. A manual procedure was then carried out to mark the electrodes in the co-registered CT space using the CTMR toolbox. The coordinates of each electrode were transformed to MRI space (1mm resolution). Since we used bipolar derivations, we computed the coordinates of the mid-point between pairs of adjacent electrodes. A cube of 5mm in size was placed at these positions (i.e., at the position of the bipolar derivation) and each voxel of the cube (1mm resolution) was labeled according to *MarsAtlas*. The location of each bipolar derivation was then labelled according to the label associated to the largest number of voxels within the cube. Bipolar derivations labelled in the white matter were excluded from further analyses.

Similarly to MEG HGA estimation, single-trial power estimates in the high-gamma range (60-120Hz) aligned on movement and stimulus onset were log-transformed and low-pass filtered at 50Hz to reduce noise. Single-trial estimates of high-gamma power were z-transformed with respect to baseline period from -0.5 and -0.1 s prior to stimulus onset. Finally, single-trial HGA for each labelled brain region of *MarsAtlas* was defined as the mean z-transformed power values averaged across all electrodes within the same region.

## Single-trial Functional Connectivity Dynamic (FCD) measures

Power modulations in the high-gamma range reflect the activity of local neural populations (Ray et al., 2008; Ray and Maunsell, 2011). Here, we assume that tracking statistical dependencies between HGA from different brain regions provides information about how local processing units coordinate at the large-scale level during cognitive tasks. The goal is not infer the mechanisms mediating inter-areal communication. This would require complementary approaches based on the study of role of neural oscillations and synchrony for inter-regional communication (e.g., Buzsáki & Schomburg, 2015; Fries, 2015). Rather, the aim was to map task-related FCD onto anatomical circuits. Given the sparseness of brain regions sampled with SEEG, FCD was exclusively performed for whole-brain MEG data.

We used linear correlation analysis to study the functional connectivity (FC) between brain regions. To quantify the evolution of FC over time (i.e., FCD), we computed the Pearson's correlation coefficient between pairs of HGA signals over sliding windows of 500msec, stepped every 10 msec. The same procedure was performed across all pairs of brain regions and for each trial. This resulted in a 4-dimentional FCD matrix (i.e., regions x regions x time points x trials) representing the evolution of linear correction across all pairs of brain areas from -0.7 to 0.7s around movement onset. The single-trial FCD matrix was also computed during the pre-stimulus period, from -0.8 to -0.1s prior to stimulus onset for baseline. Statistical analyses searched for significant modulations in movement-related FCD with respect to those in the prestimulus interval.

## Statistical analysis

Linear Mixed Effect (LME) model

Statistical inference of single-trial HGAs was performed using a linear mixed-effect (LME) model approach at the group level. We used a LME model, because they are particularly suited for the analysis of data collected from multiple subjects (or sessions) where it is important to take into account inter-individual variability. These models formalize the relation between a response variable and independent variables using both fixed and random effects. Fixed effects model the response variable in terms of explanatory variables as non-random quantities. For example, experimental conditions related to population mean may be considered as fixed effects. Random effects are associated with individual experimental units drawn at random from a population, which may correspond to different participants in the study (or experimental sessions). In other words, whereas fixed effects are constant, random effects are drawn from a prior known distribution. A LME model is generally expressed in matrix formulation as,

$$y = X\beta + Zb + e \quad (1)$$

where $y$ is the n-by-1 response vector and n is the number of observations. $X$ is an n-by-p fixed-effects design matrix and $\beta$ is the fixed-effect vector of p-by-1, where p is the number of fixed effects. $Z$ is an n-by-q random-effects design matrix and $b$ is a q-by-1 random-effects vector, where q is the number of random effects; $e$ is the n-by-1 observation error. The random-effects vector, $b$, and the error vector, $e$, were assumed to be drawn from independent normal distributions. Parameter estimation was performed using maximum likelihood method, using the *fitlme.m* function in the Statistical Toolbox of Matlab (The MathWorks, Inc.). In order to test for significant modulations in single-trial HGA and FCD measures around movement onset with respect to the baseline period, we used a random-intercept and random-slope LME model, which is described by,

$$y(t) = \beta_0(t) + \beta_1(t)x_j + b_{0j}(t) + b_{1j}(t)z_j + \epsilon_j(t) \quad (2)$$

where $y(t) = [y_{bl}(1), y_{bl}(2), \ldots, y_{bl}(np), y_{mv}(1,t), y_{mv}(2,t), \ldots, y_{mv}(np,t)]$.

For MEG data analysis, $y_{bl}(j)$ was a vector containing the baseline neural activity (i.e., the HGA from single brain regions or FCD values for single pairs of regions) for all trials and sessions (i.e., data from both sessions were concatenated, because they were acquired in uninterrupted succession) for subject $j = 1,2,\ldots,np$, where $np$ is the number of participants, at time instant *t*. Note that *t* does not refer to trials, but time within each trial. $y_{mv}(j,t)$ was a vector including brain activity across

all trials for subject $j$ at time $t$ with respect to movement onset.

For SEEG data analysis, statistical inference was performed at the single-participant level, due to the limited number of patients and limited sampling of *MarsAtlas* regions. However, given that the SEEG experiments were composed of two sessions acquired at different times (approximately 1 hours interval), we modeled sessions as random effects. $y_{bl}(j)$ was then a vector containing the baseline neural activity (i.e., the HGA from single brain regions) for all trials for sessions $j = 1,2$, at time instant $t$. As before, $t$ did not refer to trials, but time within each trial. $y_{mv}(j,t)$ was a vector including brain activity across all trials for session $j$ at time $t$ with respect to movement onset.

The following statistical analysis was similar for both MEG and SEEG data. The design matrices contain two columns. The first column is a vector of ones to model the intercept, and thus it was eliminated from eq. 2. The second column contains negative ones for baseline trials and ones for event-related trials, therefore modelling the change with respect to baseline, or slope, and it is referred as $x_j$ and $z_j$ in eq. 2. Thus, the first and third terms in the right-hand-side of eq. 2 model the intercepts, which correspond to the mean values between baseline and movement-related activity. The second and fourth terms model the slopes, which are the differences between baseline and movement-related activity. The $\beta_1(t)$ values are fixed across subjects, whereas the $b_{1_j}(t)$ values model the random variations across subjects (for MEG) or sessions (for SEEG). In other words, the parameter $\beta_1(t)$ models the change in neural activity (e.g., HGA or FCD for MEG data) with respect to baseline at each time point $t$ at the group level; the parameter $b_{1_j}(t)$ models the change in neural activity with respect to baseline for each participant (or sessions) *j* and therefore explains the across-subjects (or across-session) variability for MEG and SEEG data, respectively. The across-subject and across-session variability was considered of no interest for the scope of the current analyses. We thus analyzed fixed-effects. Given the structure of the fixed-effect design matrix, significant differences in movement-related neural activity with respect to baseline can thus be inferred by testing whether $\beta_1$ coefficients are significantly greater than zero. More formally, the significance of movement-related modulations was inferred using a t-test by testing the null hypothesis $H_0$: $\beta_1 \leq 0$.

Statistical inference was performed for each time point $t$ and each brain area

for the analysis of HGAs. To account for the multiple comparisons problem, we controlled the false discovery rate (FDR) (Benjamini and Yosef, 1995). For mean HGA statistical analyses, we corrected for the number of time points and brain regions; for FCD analyses, we corrected for the number of time points and for the number of pairs of brain regions. To further assess the validity of our results, we quantified the minimum number of consecutive significant time points required to reject a null hypothesis of absence of a cluster given a chance probability $p_0$ = 0.5 (two possible outcomes, significant or non-significant), and kept only those clusters whose duration exceeded a given significance level. Details of the calculation are given in the appendix of (Smith et al., 2004).

The statistical analyses of MEG HGA modulations resulted in a group-level FCD matrix containing time-evolving t- and p-values for each brain region in *MarsAtlas* (whole-brain analysis). For brain regions covered by the SEEG implants, the analysis of HGA modulations produced intracranial validation at the single-participant level. The analysis of FCD from MEG HGA produced t- and p-value time courses for all pairs of brain regions.

## Graph theoretical analysis

Strength of Functional Link (SFL)

To gain insight into the topology of the task-related functional network arising from group-level MEG analyses, we performed graph theoretical analyses of the FCD matrix containing the p-values associated with the LME analysis. The weight or strength of the evidence of a functional link was defined as the minimum Bayes Factor (BF) associated with such p-values (Goodman, 1999b). The rationale behind the transformation of p-values to minimum Bayes Factors is an attempt to move towards statistical measures that can be better interpreted (Goodman, 1999a). The BF is a convenient measure of the strength of statistical evidence and it can be computed from p-values as $BF_{up} < -1/(e\ p\ \ln(p))$, if $p$-values satisfy the relation $p <$ 1/e, in which $e \approx 2.72$. This estimate provides an upper bound ($BF_{up}$) on the BF, and it can be thought as providing an 'optimistic' limit of the BF for a given $p$-value (Goodman, 2001; Stephens and Balding, 2009). We log-transformed the BFs so to give a measure which quantifies the strength in the evidence of the presence of a functional link between two brain regions, Strength of the Functional Link $SFL =$

463 $\log_{10} BF_{up}$. The *SFL* matrix has the same dimensions of group-level FCD matrix (i.e.,
464 regions x regions x time points). A value between 1 and 2 can be interpreted as
465 providing strong to very strong evidence of a functional link (i.e., increase in
466 correlation with respect to baseline), whereas a value higher than 2 is interpreted as
467 decisive.
468
469 Analysis of time-averaged and time-dependent SFL
470 A caveat of FC analysis is the dependence of functional links on the threshold
471 chosen for statistical significance. Thus, to explore how graph theoretical measures
472 vary according to significance levels, we multiplied the *SFL* matrix with different
473 binary masks obtained from the FDR-correction of the FCD matrix over a wide range
474 from highly significant values ($p_{FDR\text{-}corrected}$ = q < 0.001) to non-significant (q <
475 0.99999). Note that a FDR adjusted p-value is denoted as q-value. This produced
476 several thresholded *SFL* matrices, each one associated with a given level of
477 significance.
478 As a first analysis, we computed the mean *SFL* matrices over time, thus giving
479 an adjacency matrix (regions x regions) representing the mean strength between
480 brain regions at different significance levels. We computed the density *D* (the ratio
481 between the number of functional links and the number of possible connections) as a
482 function of the q-value. In addition, to identify the most important brain regions in
483 average *SFL* graph, we computed the strength of each region (sum of functional links
484 of a region) and two indicators of centrality, such as the eigenvector centrality *EC*,
485 defined as the absolute value of the eigenvector associated with the largest
486 eigenvalue of the adjacency matrix W and it measures the importance of a region,
487 and the betweeness centrality *BC,* equal to the fraction of all shortest paths that pass
488 through a given region, so it measures the number of times a region acts as a
489 “bridge”. These measures were, however, computed only at q < 0.05. Finally, to
490 evaluate the evolution of density of the thresholded FCD, we computed it for each
491 time slice rather over the averaged FCD. Graph theoretical measures were computed
492 using the Brain Connectivity Toolbox (Rubinov & Sporns, 2010).
493
494 Detection of functional sub-networks
495 A critical step in the analysis of brain networks is the detection of communities,
496 which may correspond to functional subnetworks. Subnetworks, however, may

overlap spatially, such that a given brain region may belong to more than one group. Link communities, defined as groups of links rather than nodes, provide an appropriate framework for capturing the relationships between overlapping communities while revealing hierarchical organization (Ahn et al., 2010). To detect time-varying link communities, we used an approach based on the analysis of the correlation of edge weights over time, rather than nodes, similarly to previous works analyzing "cross-links" or "hyper-edges" (Bassett et al., 2014; Davison et al., 2015).

First, we computed the Pearson linear correlation between significant (at $q < 0.05$) pairs of *SFL* time courses. This produced an adjacency matrix (number of links in size) representing the temporal correlation between functional links. Secondly, we searched for the optimal subdivision of such graph into groups of links. To do so, we used the Louvain method (Blondel et al., 2008) that attempts to optimize the "modularity" of a partition of the network. The Louvain algorithm for modularity maximization is a non-deterministic heuristic, and therefore needs to be initialized with random seeds. In addition, it depends on the resolution parameter $\gamma$ which controls over the size and number of communities found (resolution equal to 1 leads to the standard Louvain method, whereas higher and lower resolutions produce larger and smaller number of clusters, respectively). We scanned different resolution parameters from $\gamma = 0.5$ to $\gamma = 1.5$ in increments of 0.1. At each scale, we ran the Louvain method 250 times to test whether the non-deterministic nature of the method could produce non-robust results. For all pairs of partitions (250*249 in total), we computed their similarity, defined as the z-score of the Rand index (Traub et al., 2011) and we averaged them across all pairs of partitions. The optimal resolution parameter $\gamma$ was associated with the largest average similarity between partitions. The largest similarity was observed at $\gamma = 1$. For $\gamma = 1$, we studied the consensus partition to identify a single representative partition from a set of 250 partitions, based on statistical testing in comparison to a null model. The representative partition is obtained by using a generalized Louvain algorithm on the thresholded nodal association matrix (Bassett et al., 2013). We found that for our FCD matrix at $\gamma = 1$, the Louvain algorithm is extremely stable and the 250 partitions are all identical. These graph theoretical analyses were performed using the “Consensus and Comparison Methods” in the Network Community Toolbox (http://commdetect.weebly.com/).

530 This approach provides a subdivision of non-overlapping communities by
531 maximizing the number of within-group edges and minimizing the number of
532 between-group edges. Given that community detection was performed on links, the
533 detected communities represent link communities where individual brain areas may
534 participate in multiple overlapping networks. Finally, we computed the mean time-
535 course of the SFL averaged across all links comprising each link community.

# RESULTS

## Visuomotor-related functional network

The brain regions displaying a significant increase in movement-related HGA with respect to the mean baseline (averaged from -0.5 to -0.1s prior to stimulus onset) defined the arbitrary visuomotor-related network (Figure 2). For cortical regions, the largest increase in HGA was observed over the left parietal lobe, primarily over the dorsal (dorsal intraparietal cortex, IPCd, and the superior parietal cortex, SPC) and medial (medial superior and medial parietal cortices, SPCm and PCm, respectively) parietal regions, the dorsal somatosensory areas (Sdl and Sdm) and the posterior cingulate cortex (PCC). The ventral regions, such as (IPCv and Sv), displayed a smaller increase relative to the dorsal and medial territories in the left hemisphere and were not significant in the right hemisphere. Over the motor, premotor and prefrontal areas, the dorsolateral and dorsomedial regions (PFcdl, PFcdm, PMdl, PMdm, Mdl and Mdm) showed the most significant increase. In addition, the mid-cingulate cortex (MCC) showed significant response, bilaterally. The ventral and ventromedial prefrontal and orbitofrontal cortices did not display a strong increase in HGA, nor anterior temporal regions. These cortical modulations are similar to those presented in a previous paper (Auzias et al., 2016), which we replicate them here for completeness.

The novel finding, however, is the presence of significant HGA modulations in subcortical areas. The strongest response was observed in the left hemisphere in the dorsal striatum (caudate nucleus and putamen), globus pallidus (GP) and thalamus (Thal). The thalamus and caudate nucleus displayed a clear bilateral activation, whereas the GP and putamen showed primarily an activity in the hemisphere contralateral to the motor response. A significant response was also observed in the right thalamus and caudate nucleus. No significant increase was seen in other subcortical areas examined such as the nucleus accumbens, amygdala and hippocampus.

## Visuomotor-related functional connectivity dynamics

The analysis of Functional Connectivity Dynamics (FCD) between all pairs of brain regions of *MarsAtlas* was performed by estimating Pearson's correlation

coefficients between pairs of single-trial HGA values over sliding windows of 500 msec, stepped every 10 msec. For each participant, FCD analysis resulted in a 4-dimentional matrix (i.e., regions x regions x time points x trials) representing the evolution of linear correlation across all pairs of brain areas from -0.7 to 0.7s around movement onset. Significant modulations in movement-related FCD with respect to those in the baseline period from -0.8 to -0.1s prior to stimulus onset using a linear mixed-effect (LME) approach. Figure 3A shows the connectivity matrix of the average SFL (i.e., Strength of Functional Link) over time. Note that p-values were thresholded at $q < 0.05$ (FDR-corrected) previous to SFL computation, which corresponds to a threshold value of SFL equal to 2.43. All significant links shows decisive evidence in FC averaged over time among occipital areas bilaterally with strong links with parietal regions, in addition to the fronto-parietal network. Subcortical regions, especially in the left hemisphere, showed a strong FC with the rest of the network. Regions in the temporal lobes, however, were not found to play a key role in the FC patterns.

To better characterize the evolution of the SFL over time, we computed the mean SFL across pairs of brain regions displaying a significant increase in linear correlation (Fig. 3B). The mean time course displays two peaks of decisive and strong evidence at approximately -0.4 and 0.2s around finger movement. The time intervals around the two peaks represent moments when FC pattern is strongest, which correspond to the largest increase in linear correlation between HGA time courses. Given the shape of the group-level HGA responses shown in Figure 2, the first peak at -0.4s reflects the positive covariation in HGA across the whole network occurring after stimulus presentation and during movement planning (as early as -0.55 in visual areas to approximately -0.25s before finger movement). Such common increase in HGA produces an increase in linear correlation and it reflects the emergence of the FC network. The second peak occurring at 0.2s reflects a common return to baseline of the HGA across the whole network after finger movement (from approximately 0.05s to 0.35s after finger movement). Such global decrease in HGA from maximal activity produces an increase in linear correlation, but it reflects the dissolution of the FC network. Thus, the two peaks correspond to the emergence and dissolution of the FC pattern. The decrease in FC occurring approximately -0.12s to -0.03s before finger movement corresponds to the positive peak of HGA (Fig. 2). Such decrease in FC, therefore, does not reflect an absence of HGA, but rather a maximum of HGA. However, it corresponds to the time interval when FC lacks any

significant covariation. Overall, the analysis of the FCD time course reveals two key processes such as the creation and dissolution of FC network.

## Graph theoretical analysis of FC network

To gain insight into the properties of the average FC pattern, we performed graph theoretical analyses of the average SFL matrix shown in Fig. 4A. We investigated graph theoretical measures of the mean *SFL* matrices averaged over time at different thresholds ($q < 0.001$) to non-significant ($q < 0.99999$). Figure 4A shows the FC network density *D* (the ratio between the number of functional links and the number of possible connections) as a function of threshold q-values. The density of the functional network trivially increase as a function of the threshold, i.e., the more functional links, the higher is the density. The density values for significant $q < 0.05$ are less than 10%, meaning that the functional network is not dense, but sparse. We then computed the density for each time slice of the FCD. Network density is maximal (approximately 5%) approximately 0.4 s and then displays a second peak 0.2 after finger movement (2% in density), as shown in Figure 4B.

Finally, to identify the most important brain regions in the average *SFL* graph, we computed the strength *S* (sum of functional links of a region), the eigenvector centrality *EC* and the betweeness centrality *BC* at $q < 0.05$. The strength of a brain area is the simplest measure to estimate the importance of a node in a network. A natural extension of strength centrality is eigenvector centrality *EC*, and it stands on the notion that a node is important if it is linked to by other important nodes. In fact, a node receiving many links (i.e., high strength) does not necessarily have a high eigenvector centrality, because it may be linked to node with low strength. Thus, EC provide additional information, because it computes the centrality of a node as a function of the centralities of its neighbors. Finally, the betweeness centrality *BC* is equal to the number of shortest paths that pass through a brain region. Thus, a region with high *BC* has the potential to play a key role in the network. Convergence of these three metrics provides information about the importance of different brain regions in the network.

Table 1 shows the brain regions sorted in a descending order according to *S*, *EC*, and *BC*. The brain areas that commonly emerge as relevant across the three measures are the dorsomedial and dorsolateral sensorimotor regions (Mdm, Mdl,

Sdm), in addition to dorsolateral premotor area (PMdl), superior parietal regions (SPC, SPCm) and the caudomedial visual cortex (VCcm).

## Dynamic reconfiguration of functional connectivity subnetworks

To search for functional subnetworks generating the observe dynamics, we performed link community analysis. To do so, we first computed the Pearson linear correlation between significant (at $q < 0.05$) pairs of *SFL* time courses. Then, we found the optimal subdivision of such link graph into communities of links using an algorithm that attempts to optimize the "modularity" of a partition of the network, named the Louvain method (Blondel et al., 2008). This approach provides a subdivision of non-overlapping communities by maximizing the number of within-group edges and minimizing the number of between-group edges. Given that community detection was performed on links, the detected sub-networks represent link communities, where individual brain areas may participate in multiple overlapping networks. The analysis revealed the presence of 3 link communities (Figure 5). The first link community (LC1) primarily included the visual and superior and medial parietal regions, bilaterally, in addition to the left dorsomedial and dorsolateral sensorimotor regions (Fig. 5B). These brain regions form a FC subnetwork emerging approximately 0.5s before finger movement, roughly corresponding to the processing of the visual cue (Fig. 5A). The second link community (LC2) included the left dorsolateral and dorsomedial sensorimotor regions and the dorsal fronto-parietal network. Interestingly, it included the mid and anterior cingulate cortices, the dorsomedial prefrontal cortex and the dorstal striatum, in the caudate nucleus (Fig. 5C). LC2 emerged later during the trial and its maximum of expansion occur approximately 100-150 msec after LC1, that is -0.35s before movement. LC3 involved a larger brain network involving the bilateral sensorimotor regions, the left fronto-parietal network and visual areas (Fig. 5D). LC3 showed a strongest peak after finger movement at 0.2s, but displays a peak at -0.4s. The only regions of the temporal lobe showing significant FC were the superior and mid-temporal cortices in the left hemisphere. However, these regions displayed a relative weak strength in the observed networks (Figure 5B, C and D). Overall, the link community analyses allowed us to identify multiple and spatially overlapping FC patterns that evolve dynamically during the trial.

We can therefore depict the involvement of key brain regions in a given link community, such as the motor and premotor areas. Figure 6 shows the contribution of the dorsolateral motor and dorsal premotor areas, Mdl and PMdl, respectively, in the three subnetworks as it unfolds over time. Around the presentation of the visual stimulus, the Mdl primarily participates in the LC1, which gradually declines over time (blue curve in Fig. 6A and B). Then, its involvement in LC2 and LC3 increases in parallel, but peaks earlier for LC2 (red curve in Fig. 6A and B) rather than for LC3 (green curve). These curves depict the dynamic reconfiguration of the primary motor area from stimulus onset to motor output. For what concerns the dorsolateral premotor cortex, its contribution peaking for LC1, followed by LC3 and LC2 (Fig. 6C and D) confirms that the dynamic engagement in different subnetworks occurs over a short time scale.

Finally, to quantify the dynamics of reconfiguration among the three functional subnetworks, we inferred the evolution of network "flexibility" (following the same ideas developed in Braun and collaborators, 2015). We defined the flexibility of a given brain region as the entropy associated to the probabilities of involvement in the three LCs (shown in Fig. 6B and D, for Mdl and PMdl, respectively). Accordingly, node flexibility is maximal for nodes participating with equal probability in the different LCs and minimal for nodes participating in a single LC. Figure 7A shows the mean dynamics of network flexibility averaged over nodes. Interestingly, it reconfiguration shows a single peak occurring at approximately 0.4s before finger movement, which corresponds to the moment when the three LCs overlap more strongly in time and space. Figure 7B shows the mean flexibility averaged over time for the first five strongest brain regions. The parietal regions (SPC, PCm and PPC) display the largest flexibility together with the dorsal premotor cortex.

## Control analyses and intracranial SEEG validation

The interpretation of FC measures from non-invasive techniques such as EEG and MEG may suffer limitations, among which volume conduction and leakage are potential confounds (Bastos & Schoffelen, 2016). We performed a series of control analyses to assess the influence of such confounds.

First, we studied the relation between the mean SLF for two subcortical regions displaying a significant increase in HGA and FC with cortical regions, as a

function of their respective distance to cortical regions. The rationale was to check whether volume conduction and leakage effects could have produced the observed HGA modulations in subcortical reasons and the FC patterns between deep sources, such as the thalamus and caudate nucleus, and cortical areas. Figure 8 shows that a clear relation between distance and FC measures (as assessed through the mean SFL) is lacking, neither for the thalamus (Fig., 8A) nor for the caudate nucleus (Fig. 8B).

Second, we investigated the dipole orientation of all sources within the thalamus and caudate nucleus. The rationale was that differences in dipole orientation of nearby regions may suggest that the estimated HGAs originate from spatially-separable brain structures. To do so, we computed the average dipole orientation both for the thalamus and caudate nucleus. Then, we compared the average dipole orientations by means of the normalized inner product. This measure equals one for identically-oriented dipoles, minus one for dipoles pointing in opposite directions, and zero for orthogonal dipoles. The boxplot displayed in Figure 9A depicts the distribution of normalized inner products between the thalamus and caudate nucleus across participants. The values of normalized inner products span a broad range from -0.45 to 0.85, with median value around 0.65. Extremely high values of raw correlation coefficient between subcortical HGAs would also suggest strong leakage effects. We thus plotted the Pearson correlation coefficient between the HGA at the thalamus and caudate nucleus, averaged over sessions and participants (Figure 9B). The value in the prestimulus interval (i.e., approximately around -0.8s before finger movement) was 0.615. The corresponding coefficient of determination $R^2$ was 37,8%, (i.e., $R^2$ = 0.615 x 0.615 = 0.3782), and it equals the proportion of the variance in HGA shared by the thalamus and caudate nucleus.

Finally, to assess the relevance of cortical HGA modulations, we asked three patients candidate for surgical treatment of drug-resistant epilepsy to perform the same visuomotor task while recording stereotactic electroencephalography (SEEG) in multiple brain areas. In fact, high-gamma activity from intracranial recordings in epileptic patients is largely exploited for cognitive mapping and it represents an optimal opportunity to validate MEG results. Results from single-patient SEEG cannot be taken as representative of the population, contrary to group-level MEG results. In fact, we cannot exclude that across-subject variability is due to either physiological and/or pathological factors. However, SEEG data provide direct measures of

735 intracranial HGA, free from alteration due to volume conduction or limitation of source
736 imaging tools. Thus, they provide important additional evidence to support the
737 significance of the MEG results.

738 Electrodes were localized by combing post-implant CT scans with pre-surgical
739 anatomical MRI scans, and they were labelled according to *MarsAtlas* (see methods
740 section). Single-trial HGA for each labelled brain region of *MarsAtlas* was defined as
741 the mean z-transformed power values averaged across all electrodes within the
742 same region. To increase the local specificity of SEEG recordings, bipolar derivations
743 were performed among adjacent contacts. Statistical analyses were performed
744 separately for each patient. Twelve brain areas across the three patients were found
745 to display a significant increase in HGA (Table 2) ($q < 0.05$). These included the
746 dorsomedial and dorsolateral motor cortex, the dorsolateral somatosensory region,
747 and the dorsal fronto-parietal network (SPC, SPCm, PMdl, PMdm). In patient 2, the
748 ventral portions of the motor and premotor areas were significantly active. Note that
749 the SEEG implant did not cover the entire brain, but selected regions in the fronto-
750 parietal network.

751 We then compared the average time course of single-patient HGA
752 modulations with those from the MEG group-level analyses (Fig. 10). Seven out of
753 twelve regions displayed a strong (larger than 0.65) linear correlation between the
754 group-level MEG results and the single-patient SEEG time courses. The most striking
755 similarity was observed for brain regions of the sensorimotor cortices and the dorsal
756 fronto-parietal network. Overall, these results confirm that the increase in HGA
757 observed in the MEG data over sensorimotor cortices and the dorsal fronto-parietal
758 network results from area-specific increases in HGA, rather than by leakage from
759 nearby regions displaying a strong response.

# DISCUSSION

## Brain network and interactions of visuomotor mapping

Previous analyses of arbitrary visuomotor-related functional connectivity have shown that parietal areas play a driving role in the network, whereas premotor areas act as relays from parietal to medial prefrontal cortices, which participate as receivers (Brovelli et al., 2015). Such approach, however, neither considered the time-evolving nature of FC patterns, nor analyzed the involvement of subcortical areas. Our whole-brain and time-dependent brain connectivity analyses showed that visuomotor mapping resides in three distinct and partly overlapping subnetworks with time-evolving cortico-cortical and cortico-subcortical interactions. Approximately 0.5s before finger movement, visual and parietal regions coordinate with sensorimotor and premotor areas (LC 1 in Fig. 5B; blue curve in Fig. 5A). Subsequently, the sensorimotor regions, the dorsal fronto-parietal circuit, the medial prefrontal regions, the basal ganglia and the thalamus (LC 2 in Fig. 5C) dominated the FC pattern. The dorsal fronto-parietal circuit, known to support visuomotor transformations and goal-directed attentional processes (Wise et al., 1996; Wise and Murray, 2000; Corbetta and Shulman, 2002; Culham and Valyear, 2006), is tightly coupled with the sensorimotor and associative fronto-striatal circuit for a brief period around 0.35s prior to action (red curve in Fig. 5A). This FC network includes medial prefrontal areas, such as the dorso-medial prefrontal cortex (PFCdm), mid-cingulate cortex (MCC), anterior cingulate cortex (ACC) and rostro-medial prefrontal (PFrm), with a strongest increase in HGA in the MCC and PFCdm (Fig. 2). The involvement of medial prefrontal areas may correspond to the activation of visuomotor-related neural populations of the rostral cingulate zone (RCZ), a key node of the human motor system (Picard and Strick, 1996; Amiez and Petrides, 2014). At the subcortical level, the dorsal striatum (caudate nucleus and putamen), globus pallidus and thalamus displayed the strongest HGA, in the hemisphere contralateral to the motor response (Fig. 2). Indeed, intracranial recordings from patients with motor disorders have described HGA in the subthalamic nucleus (Amirnovin et al., 2004; Alegre et al., 2005; Androulidakis et al., 2007; Lalo et al., 2008), globus pallidus (Tsang et al., 2012a) and thalamus (Brucke et al., 2013) during different types of motor behaviors. High-gamma oscillatory activity in the sub-thalamic nucleus (STN) and globus

pallidus (GPi) has been found to be coherent with cortical activity during voluntary movement (Cassidy et al., 2002; Brown, 2003). Granger causality analysis also showed that STN drives activity in M1 (Litvak et al., 2012), thus suggesting that HGA in motor areas is due to propagating activity from the basal ganglia through the thalamus (Brucke et al., 2012). Our results showed that the caudate nucleus and thalamus are coupled with the sensorimotor cortex and the dorsal fronto-parietal networks (LC 2 in Fig. 5C), thus confirming a dynamic coordination between cortical and subcortical regions also during visuomotor behaviors most prominently during the planning phase prior to movement initiation.

Several lines of evidence suggest that the reported subcortical activations are primarily local, rather than due to leakage from cortical areas. First, we observed that the putamen significantly activated only in the left hemisphere, whereas the thalamus was activated bilaterally (Fig. 2). If the bilateral activation in the thalamus were due to leakage from cortical areas, we would have expected a bilateral activation also in the putamen, given that the thalamus is deeper than the putamen. Second, no significant correlation was found between the SFL and distance for the thalamus and caudate nucleus (Fig. 8). Third, the average dipole orientation for the thalamus and caudate nucleus are significantly different (i.e., the normalized inner product is less than one) and the distribution of values covers a wide range from -0.45 to approximately 0.85. This suggests that the thalamus and caudate nucleus lack a systematic similarity in dipole orientation (Fig. 9A). Forth, the mean Pearson correlation values and the corresponding coefficient of determination do not saturate at high values and show a modulation similar to the average time course of FCD (Fig. 9B). This suggests a lack of strong covariance, as it would be expected if leakage effects were dominating.

Nevertheless, we cannot *apriori* exclude that the observed subcortical increases in HGA and FC patterns may be due to complex configurations of cortical activations. Indeed, we suggest that HGA estimation at subcortical areas and FC analysis should not be performed blindly. Rather, the analysis of raw correlations and dipole orientations provide important insight into the origin of the results. Experimentally, simultaneous MEG and subcortical measures of HGA from intracranial recordings would be required to confirm or disprove the ability of MEG to capture subcortical HGA and FC.

Overall, our result suggests that the basal ganglia form a dynamic functional network, which may allow the coordination within and across different processing

streams in the basal ganglia (Brown, 2003) and facilitate motor output (Cheyne and Ferrari, 2013). The involvement of sensorimotor and associative fronto-striatal circuits, classically thought to be involved in habits (Yin and Knowlton, 2006; Graybiel, 2008; Ashby et al., 2010), also suggests that performance of arbitrary visuomotor mappings can be viewed as a form of acquainted instrumental behavior (Brovelli et al., 2015), whose gradual consolidation would lead to the formation of habitual responses (Dickinson, 1985; Dickinson and Balleine, 1993). We therefore suggest that the FCD pattern observed for LC2 depicts how motor plans circulate in the sensorimotor and associative cortico-striatal loop in coordination with fronto-parietal circuits.

Finally, a last subnetwork (LC 3 in Fig. 5D) primarily emerging after motor response peaking around 0.2s (green curve in Fig. 5A), involved the bilateral sensorimotor regions, the left fronto-parietal network and visual areas. The involvement of bilateral sensorimotor regions indicates that this network mediates cortico-cortical interhemispheric coordination processes via the corpus callosum. Such interhemispheric coupling may support the selective inhibition of inappropriate responses occurring between motor and premotor cortices across hemispheres in situations when multiple choices are available (Duque et al., 2013; Burle et al., 2016). Alternatively, this network may be involved in the processing of the somatosensory reafference at the end of the movement and/or the processing action's outcome.

To exclude potential confounds due to volume conduction or limited spatial resolution of MEG and beamforming technique (Bastos & Schoffelen, 2016), we showed that local field potentials derived from SEEG recordings displayed significant increase in HGA in these regions (Fig. 10, Table 2). We confirmed invasively that brain regions of the dorsal fronto-parietal network and the sensorimotor and/or associative fronto-striatal circuits display local increase in HGA, which do not result from volume conduction effects.

## Towards a better understanding of cognitive architectures

We computed the density of the thresholded FC and FCD graphs as a function of significance threshold (Fig. 4) using the FDR-controlling procedure to estimate the relevant range of q-values. For $q < 0.05$, the density of the visuomotor-related FC network is less than 10% (approximately 5% for $q < 0.05$). This shows that

visuomotor-related FC is not dense, but sparse. Future work on the relation between structural and functional connectivity may provide clues of how anatomical connectivity between brain areas shapes how neural information flows and constrains the dynamics of FC patterns.

A second characteristic of FC is its non-stationarity nature. Indeed, fMRI investigations have shown that resting-state networks (RSNs) display non-stationarity and dynamically evolve over tens of seconds to minutes (Hutchinson et al., 2013; Yeo et al., 2013; Allen et al., 2014; Cole et al., 2014; Calhoun et al., 2014; Zalenski et al., 2014; Hansen et al., 2015). Inter-areal phase-synchronisation is known to display non-stationarity, and to underlie perception and executive functions (e.g., Pesaran et al., 2008; Hipp et al., 2011; Salazar et al., 2012). Our results further support the notion that FC is non-stationary and evolves over time scales relevant for visuomotor integration in the order of tens to hundreds of milliseconds (Fig. 3B and Fig. 5). Modelling studies of resting-state activity suggest that non-stationarity arises from the out-of-equilibrium sampling of alternative dynamical modes (Deco & Jirsa, 2012; Hansen et al., 2015; Deco et al., 2015). Switching between collective dynamical states have the potential to induce network-wide reorganization of information sharing and routing patterns and, thus, provides an effective mechanism for flexible inter-areal communication (Battaglia et al., 2012; Kirst et al., 2016). We suggest that such underlying mechanisms mediating spontaneous large-scale dynamics may also underlie task-related activity at shorter time scale. In addition, our results may provide the basis for linking similar patterns of FCD that have been observed, albeit over different time scales, during visuomotor learning (Bassett et al., 2011; Heitger et al., 2012).

A third characteristic of FCD is the presence of multiple and spatially overlapping sub-networks. Each brain area can participate in multiple sub-networks depending of task demands. In analogy to the concept of cell assembly, where single neurons can participate in multiple functional populations depending on context, a sub-network may be viewed as a brain assembly. A brain assembly would constitute a dynamic entity, whose constituents engage in multiple sub-networks in a time-dependent manner (Fig. 6). Spatially, areal flexibility was larger for associative parietal regions, such as the SPC, PCm and PPC together with the dorsal premotor cortex, which represent the core cortical network for visuomotor transformation (Fig. 7B). Temporally, network flexibility showed a maximum around 0.4s before finger

movement, which corresponds to the moment when the three sub-networks interact more strongly (Fig. 7A). We therefore suggest that visuomotor integration processes occur in this time interval, when the level of interactions between multiple brain assemblies is strongest.

To conclude, our study confirms that executive functions arise from the dynamic coordination of neural activity over large-scale networks (Varela et al., 1999; von der Malsburg et al., 2010; Bressler and Menon, 2010). More precisely, the results supports the notion that functional specialization is due to the interplay of multiple and spatially overlapping subnetworks, rather than properties of single brain regions (Fedorenko and Thompson-Schill, 2014; Petersen and Sporns, 2015). Future work investigating how subnetworks differently participate depending on tasks demands may provide a better understanding of the cognitive architectures of executive functions (Dehaene et al., 2015).

# REFERENCES


Ahn Y-Y, Bagrow JP, Lehmann S (2010) Link communities reveal multiscale complexity in networks. Nature 466:761–764

Alegre M, Alonso-Frech F, Rodriguez-Oroz MC, Guridi J, Zamarbide I, Valencia M, Manrique M, Obeso JA, Artieda J (2005). Movement-related changes in oscillatory activity in the human subthalamic nucleus: ipsilateral vs. contralateral movements. Eur. J. Neurosci. 22, 2315–2324.

Androulidakis AG, Kuhn AA, Chen CC, Blomstedt P, Kempf F, Kupsch A, Kupsch A, Schneider GH, Doyle L, Dowsey-Limousin P, Hariz MI, Brown P (2007). Dopaminergic therapy promotes lateralized motor activity in the subthalamic area in Parkinson's disease. Brain 130, 457–468.

Allen EA, Damaraju E, Plis SM, Erhardt EB, Eichele T, Calhoun VD (2014). Tracking whole-brain connectivity dynamics in the resting state. Cereb Cortex. 24(3):663-76.

Amiez C, Petrides M (2014) Neuroimaging evidence of the anatomo-functional organization of the human cingulate motor areas. Cereb Cortex 24:563–578.

Amirnovin R, Williams ZM, Cosgrove GR, Eskandar EN (2004). Visually guided movements suppress subthalamic oscillations in Parkinson's disease patients. J. Neurosci. 24, 11302–11306.

Ashby FG, Turner BO, Horvitz JC (2010). Cortical and basal ganglia contributions to habit learning and automaticity. Trends Cogn Sci. 2010 May;14(5):208-15.

Auzias G, Lefèvre J, Le Troter A, Fischer C, Perrot M, Régis J, Coulon O (2013). Model-driven harmonic parameterization of the cortical surface: HIP-HOP. IEEE Trans Med Imaging. 32(5):873-87.

Auzias G, Coulon O, Brovelli A (2016). MarsAtlas: A cortical parcellation atlas for functional mapping. Hum Brain Mapp. 37(4):1573-92.

Ball T, Demandt E, Mutschler I, Neitzel E, Mehring C, Vogt K, Aertsen A, Schulze-Bonhage A (2008) Movement related activity in the high gamma range of the human EEG. Neuroimage 41:302–310.

Bassett DS, Wymbs NF, Porter MA, Mucha PJ, Carlson JM, Grafton ST (2011). Dynamic reconfiguration of human brain networks during learning. Proc Natl Acad Sci U S A. 108(18):7641-6.

939 Bassett DS, Porter MA, Wymbs NF, Grafton ST, Carlson JM, Mucha PJ (2013).
940 Robust detection of dynamic community structure in networks. Chaos, 23, 1.
941 Bassett DS, Wymbs NF, Porter MA, Mucha PJ, Grafton GT (2014). Cross-linked
942 structure of network evolution. Chaos, 24:013112.
943 Bastos AM, Schoffelen JM (2016). A Tutorial Review of Functional Connectivity
944 Analysis Methods and Their Interpretational Pitfalls. Front Syst Neurosci. 8;9:175.
945 Battaglia D, Witt A, Wolf F, Geisel T (2012) Dynamic Effective Connectivity of Inter-
946 Areal Brain Circuits. PLoS Comp Biol 8:e1002438.
947 Benjamini Y, Yosef H (1995) Controlling the False Discovery Rate : A Practical and
948 Powerful Approach to Multiple Testing. Journal of the Royal Statistical Society.
949 Series B (Methodological), 57:289-3001.
950 Blondel VD, Guillaume JL, Lambiotte R, Lefebvre E (2008). Fast unfolding of
951 communities in large networks. Journal of Statistical Mechanics: Theory and
952 Experiment (10), P1000
953 Braun U, Schäfer A, Walter H, Erk S, Romanczuk-Seiferth N, Haddad L, Schweiger
954 JI, Grimm O, Heinz A, Tost H, Meyer-Lindenberg A, Bassett DS. Dynamic
955 reconfiguration of frontal brain networks during executive cognition in humans.
956 Proc Natl Acad Sci U S A. 112(37):11678-83.
957 Bressler SL, Menon V (2010) Large-scale brain networks in cognition : emerging
958 methods and principles. Trends Cogn Sci 14:277–290.
959 Brovelli, A., Lachaux, J., Kahane, P., Boussaoud, D. (2005) High gamma frequency
960 oscillatory activity dissociates attention from intention in the human premotor
961 cortex. Neuroimage 28:154–164.
962 Brovelli A, Chicharro D, Badier JM, Wang H, Jirsa V (2015). Characterization of
963 Cortical Networks and Corticocortical Functional Connectivity Mediating Arbitrary
964 Visuomotor Mapping. J Neurosci. 35(37):12643-58.
965 Brown P (2003). Oscillatory nature of human basal ganglia activity: relationship to the
966 pathophysiology of Parkinson's disease. Mov Disord. 18(4):357-63.
967 Brücke C, Bock A, Huebl J, Krauss JK, Schönecker T, Schneider GH, Brown P, Kühn
968 AA (2013). Thalamic gamma oscillations correlate with reaction time in a
969 Go/noGo task in patients with essential tremor. Neuroimage 75C, 36–45.
970 Burle B, van den Wildenberg WP, Spieser L, Ridderinkhof KR (2016). Preventing
971 (impulsive) errors: Electrophysiological evidence for online inhibitory control over
972 incorrect responses. Psychophysiology. Mar 23.

973 Buzsáki G, Schomburg EW (2015). What does gamma coherence tell us about inter-
974 regional neural communication? *Nat Neurosci*. 18(4):484-9.
975 Cachia A, Mangin JF, Rivière D, Papadopoulos-Orfanos D, Kherif F, Bloch I, Régis J
976 (2003). A generic framework for the parcellation of the cortical surface into gyri
977 using geodesic Voronoï diagrams. Medical Image Analysis, 7(4), 403–16.
978 Calhoun VD, Miller R, Pearlson G, Adalı T (2014) The Chronnectome: Time-Varying
979 Connectivity Networks as the Next Frontier in fMRI Data Discovery. Neuron
980 84:262–274.
981 Cassidy M, Mazzone P, Oliviero A, Insola A, Tonali P, Di Lazzaro V, Brown P (2002).
982 Movement-related changes in synchronization in the human basal ganglia. Brain.
983 125(Pt 6):1235-46.
984 Cheyne D, Ferrari P (2013) MEG studies of motor cortex gamma oscillations:
985 evidence for a gamma “fingerprint” in the brain? Front Hum Neurosci 7:575.
986 Cole MW, Bassett DS, Power JD, Braver TS, Petersen SE (2014). Intrinsic and task-
987 evoked network architectures of the human brain. Neuron 83(1):238-51.
988 Corbetta M, Shulman GL (2002). Control of goal-directed and stimulus-driven
989 attention in the brain. Nat Rev Neurosci. 3(3):201-15.
990 Coupe P, Yger P, Prima S, Hellier P, Kervrann C, Barillot C (2008). An optimized
991 blockwise nonlocal means denoising filter for 3-D magnetic resonance images.
992 IEEE Trans Med Imaging. 2008 Apr;27(4):425-41.
993 Crone NE, Sinai A, Korzeniewska A (2006) High-frequency gamma oscillations and
994 human brain mapping with electrocorticography. Prog Brain Res 159:275–295.
995 Culham JC, Valyear KF (2006). Human parietal cortex in action. Curr Opin Neurobiol.
996 16(2):205-12.
997 Davison EN, Schlesinger KJ, Bassett DS, Lynall ME, Miller MB, Grafton ST, Carlson
998 JM. Brain network adaptability across task states (2015). PLoS Comput Biol.
999 8;11(1):e1004029.
1000 Darvas F, Scherer R, Ojemann JG, Rao RP, Miller KJ, Sorensen LB (2010) High
1001 gamma mapping using EEG. Neuroimage 49:930–938.
1002 Dickinson A, Balleine B (1993) Actions and responses: The dual psychology of
1003 behaviour. In: Eilan, N.; McCarthy, R.A.; Brewer, B., Eds. Spatial
1004 Representation: Problems in Philosophy and Psychology. Malden, MA: Blackwell
1005 Publishers, pp. 277–293

1006 Deco G, Jirsa VK (2012) Ongoing cortical activity at rest: criticality, multistability, and
1007 ghost attractors. Journal of Neuroscience 32:3366–3375.
1008 Deco G, Tononi G, Boly M, Kringelbach ML (2015). Rethinking segregation and
1009 integration: contributions of whole-brain modelling. Nat Rev Neurosci. 16(7):430-9.
1010 Dehaene S, Dudai Y, Konen C (2015). Cognitive Architectures. Neuron. 88(1):1.
1011 Desikan RS, Ségonne F, Fischl B, Quinn BT, Dickerson BC, Blacker D, Buckner RL,
1012 Dale AM, Maguire RP, Hyman BT, Albert MS, Killiany RJ. (2006). An automated
1013 labeling system for subdividing the human cerebral cortex on MRI scans into gyral
1014 based regions of interest. NeuroImage, 31, 968–980.
1015 Dickinson AD (1985) Actions and habits: the development of behavioral autonomy.
1016 Philos Trans R Soc Lond B Biol Sci 308:67–78.
1017 Duque J, Olivier E, Rushworth M (2013). Top-down inhibitory control exerted by the
1018 medial frontal cortex during action selection under conflict. J Cogn Neurosci.
1019 25(10):1634-48.
1020 Fischl B, Salat DH, Busa E, Albert M, Dieterich M, Haselgrove C, van der Kouwe A,
1021 Killiany R, Kennedy D, Klaveness S, Montillo A, Makris N, Rosen B, Dale AM
1022 (2002). Whole brain segmentation: automated labeling of neuroanatomical
1023 structures in the human brain. Neuron 33, 341-355.
1024 Fedorenko E, Thompson-Schill SL (2014). Reworking the language network. Trends
1025 Cogn Sci. 18(3):120-6.
1026 Fries P (2015). Rhythms for Cognition: Communication through Coherence. Neuron.
1027 88(1):220-35.
1028 Goodman SN (1999a). Toward evidence-based medical statistics. 1: The P value
1029 fallacy. Annals of Internal Medicine. 130(12): 995–1004.
1030 Goodman SN (1999b). Toward evidence-based medical statistics. 2: The Bayes
1031 factor. Annals of Internal Medicine. 130(12):1005-13.
1032 Goodman SN (2001). Of P-values and Bayes: a modest proposal. Epidemiology. 12(3):295-
1033 7.
1034 Graybiel AM (2008) Habits, Rituals and the Evaluative Brain. Annu Rev
1035 Neurosci:359–387.
1036 Gross J, Kujala J, Hamalainen M, Timmermann L, Schnitzler A, Salmelin R (2001)
1037 Dynamic imaging of coherent sources: Studying neural interactions in the human
1038 brain. Proc Natl Acad Sci USA 98:694–699.
1039 Hadj-bouziane F, Meunier M, Boussaoud D (2003) Conditional visuo-motor learning

in primates : a key role for the basal ganglia. J Physiol Paris. 97:567–579.

Hansen EC, Battaglia D, Spiegler A, Deco G, Jirsa VK (2015). Functional connectivity dynamics: modeling the switching behavior of the resting state. Neuroimage.105:525-35.

Heitger MH, Ronsse R, Dhollander T, Dupont P, Caeyenberghs K, Swinnen SP (2012). Motor learning-induced changes in functional brain connectivity as revealed by means of graph-theoretical network analysis. Neuroimage. 2;61(3):633-50.

Hermes D, Miller KJ, Noordmans HJ, Vansteensel MJ, Ramsey NF (2010). Automated electrocorticographic electrode localization on individually rendered brain surfaces. Journal of neuroscience methods.185:293–298.

Hipp JF, Engel AK, Siegel M (2011) Oscillatory synchronization in large-scale cortical networks predicts perception. Neuron 69:387–396.

Hutchison RM, Womelsdorf T, Allen EA, Bandettini PA, Calhoun VD, Corbetta M, Della Penna S, Duyn JH, Glover GH, Gonzalez-Castillo J, Handwerker DA, Keilholz S, Kiviniemi V, Leopold DA, de Pasquale F, Sporns O, Walter M, Chang C. (2013). Dynamic functional connectivity: Promise, issues, and interpretations. Neuroimage 80, 360–378.

Jerbi K, Dalal SS, Jung J, Minotti L, Bertrand O, Berthoz A, Kahane P, Lachaux J, Bernard C (2009) Task-Related Gamma-Band Dynamics From an Intracerebral Perspective : Review and Implications for Surface EEG and MEG. 1771:1758–1771.

Ko AL, Weaver KE, Hakimian S, Ojemann JG (2013) Identifying functional networks using endogenous connectivity in gamma band electrocorticography. Brain Connect 3:491–502.

Lachaux J-P, Axmacher N, Mormann F, Halgren E, Crone NE (2012) High-frequency neural activity and human cognition: past, present and possible future of intracranial EEG research. Prog Neurobiol 98:279–301.

Lalo E, Thobois S, Sharott A, Polo G, Mertens P, Pogosyan A, Brown P (2008). Patterns of bidirectional communication between cortex and basal ganglia during movement in patients with Parkinson disease. J. Neurosci. 28, 3008–3016.

Lancaster JL, Woldorff MG, Parsons LM, Liotti M, Freitas CS, Rainey L, Kochunov PV, Nickerson D, Mikiten SA, Fox PT (2000). Automated Talairach atlas labels for functional brain mapping. *Hum Brain Mapp*, 10(3), 120–131.

1074 Litvak V, Eusebio A, Jha A, Oostenveld R, Barnes G, Foltynie T, Limousin P, Zrinzo
1075 L, Hariz MI, Friston K, Brown P (2012). Movement-related changes in local and
1076 long-range synchronization in Parkinson's disease revealed by simultaneous
1077 magnetoencephalography and intracranial recordings. J Neurosci 32, 10541–
1078 10553.
1079 Kirst C, Timme M, Battaglia D (2016) Dynamic information routing in complex
1080 networks. Nat Comms 7:11061.
1081 Mangin JF, Rivière D, Cachia A, Duchesnay E, Cointepas Y, Papadopoulos-Orfanos
1082 D, Scifo P, Ochiai T, Brunelle F, Régis J (2004). A framework to study the
1083 cortical folding patterns. Neuroimage. 23 Suppl 1:S129-38.
1084 Markov NT, Ercsey-Ravasz MM, Ribeiro Gomes AR, Lamy C, Magrou L, Vezoli J,
1085 Misery P, Falchier A, Quilodran R, Gariel MA, Sallet J, Gamanut R, Huissoud C,
1086 Clavagnier S, Giroud P, Sappey-Marinier D, Barone P, Dehay C, Toroczkai Z,
1087 Knoblauch K, Van Essen DC, Kennedy H (2014). A weighted and directed
1088 interareal connectivity matrix for macaque cerebral cortex. Cereb Cortex.
1089 24(1):17-36.
1090 Markov NT, Ercsey-Ravasz M, Van Essen DC, Knoblauch K, Toroczkai Z, Kennedy
1091 H (2013). Cortical high-density counterstream architectures. Science.
1092 1;342(6158):1238406.
1093 Mitra PP, Pesaran B (1999) Analysis of dynamic brain imaging data. Biophys J
1094 76:691–708.
1095 Murray E a, Bussey TJ, Wise SP (2000) Role of prefrontal cortex in a network for
1096 arbitrary visuomotor mapping. Exp brain Res 133:114–129.
1097 Nolte G (2003) The magnetic lead field theorem in the quasi-static approximation and
1098 its use for magnetoencephalography forward calculation in realistic volume
1099 conductors. Phys Med Biol 48:3637–3652.
1100 Passingham RE, Toni I, Rushworth MF (2000) Specialisation within the prefrontal
1101 cortex: the ventral prefrontal cortex and associative learning. Exp brain Res
1102 133:103–113.
1103 Picard N, Strick PL (1996) Motor areas of the medial wall: a review of their location
1104 and functional activation. Cereb cortex 6:342–353
1105 Onnela JP, Saramäki J, Kertész J, Kaski K (2005). Intensity and coherence of motifs
1106 in weighted complex networks. Phys. Rev. E 71:065103

1107 Pandya D.N., Yeterian E. (1985). Architecture and connections of cortical association
1108 areas, 1985. http://link.springer.com/chapter/10.1007/978-1-4757-9619-3_1
1109 Perrot M, Rivière D, Mangin JF (2011). Cortical sulci recognition and spatial
1110 normalization. Med Image Anal. 15(4):529-50.
1111 Percival DB, Walden AT (1993) Spectral Analysis for Physical Applications.
1112 Cambridge: Cambridge University Press
1113 Pesaran B, Nelson MJ, Andersen RA (2008). Free choice activates a decision circuit
1114 between frontal and parietal cortex. Nature. 453(7193):406-9.
1115 Petersen SE, Sporns O (2015). Brain Networks and Cognitive Architectures. Neuron.
1116 88(1):207-19.
1117 Petrides M (2005) Lateral prefrontal cortex : architectonic and functional organization.
1118 Philos Trans R Soc Lond B Biol Sci. 360:781-95.
1119 Ray S, Crone NE, Niebur E, Franaszczuk PJ, Hsiao SS. Neural correlates of high-
1120 gamma oscillations (60–200 Hz) in macaque local field potentials and their
1121 potential implications in electrocorticography (2008). Journal of Neuroscience.
1122 28:11526–11536
1123 Ray S, Maunsell JH (2011). Different origins of gamma rhythm and high-gamma
1124 activity in macaque visual cortex. PLoS Biol 9: e1000610.
1125 Régis J, Mangin J-F, Ochiai T, Frouin V, Rivière D, Cachia A, Samson Y (2005).
1126 “Sulcal Root” Generic Model: a Hypothesis to Overcome the Variability of the
1127 Human Cortex Folding Patterns. Neurologia Medico-Chirurgica, 45(1), 1–17
1128 Rubinov M, Sporns O (2010). Complex network measures of brain connectivity: Uses
1129 and interpretations. NeuroImage 52:1059-69.
1130 Salazar RF, Dotson NM, Bressler SL, Gray CM (2012). Content-specific fronto-
1131 parietal synchronization during visual working memory. Science. 338(6110):1097-
1132 100.
1133 Smith AC, Frank LM, Wirth S, Yanike M, Hu D, Kubota Y, Graybiel AM, Suzuki W a,
1134 Brown EN (2004) Dynamic analysis of learning in behavioral experiments. J
1135 Neurosci 24:447–461.
1136 Stephens M, Balding DJ (2009). Bayesian statistical methods for genetic
1137 associationstudies. Nat Rev Genet.10(10):681-90.
1138 Tou JT, Gonzalez RC (1974). Pattern Recognition Principles. Reading,
1139 Massachusetts: Addison-Wesley Publishing Company.

1140 Traud AL, Kelsic ED, Mucha PJ and Porter MA (2011) Comparing community
1141 structure to characteristics in online collegiate social networks. SIAM Review 53,
1142 526-543.
1143 Tsang EW, Hamani C, Moro E, Mazzella F, Lozano AM, Hodaie M, Yeh IJ, Chen R
1144 (2012). Movement related potentials and oscillatory activities in the human internal
1145 globus pallidus during voluntary movements. J. Neurol. Neurosurg. Psychiatry 83,
1146 91–97.
1147 Tzourio-Mazoyer N, Landeau B, Papathanassiou D, Crivello F, Etard O, Delcroix N,
1148 Mazoyer B, Joliot M. (2002). Automated anatomical labeling of activations in SPM
1149 using a macroscopic anatomical parcellation of the MNI MRI single-subject brain.
1150 *NeuroImage*, *15*(1), 273–89.
1151 Van Essen DC, Drury HA (1997). Structural and Functional Analyses of Human
1152 Cerebral Cortex Using a Surface-Based Atlas. J Neurosci, 17(18), 7079–7102.
1153 Varela F, Lachaux JP, Rodriguez E, Martinerie J (2001). The brainweb: phase
1154 synchronization and large-scale integration. Nat Rev Neurosci. 2(4):229-39.
1155 Veen BD Van, Drongelen W Van, Yuchtman M, Suzuki A (1997) Localization of Brain
1156 Electrical Activity via Linearly Constrained Minimum Variance Spatial Filtering.
1157 IEEE Trans Biomed Eng. 44:867-80
1158 Vidal JR, Chaumon M, O'Regan JK, Tallon-Baudry C (2006) Visual grouping and the
1159 focusing of attention induce gamma-band oscillations at different frequencies in
1160 human magnetoencephalogram signals. J Cogn Neurosci 18:1850–1862.
1161 Von der Malsburg C, Phillips PEM, Singer W (2010). Dynamic Coordination in the
1162 Brain (MIT Press)
1163 Wise SP, Pellegrino G, Boussaoud D (1996) The premotor cortex and nonstandard
1164 sensorimotor mapping. Can J Physiol Pharmacol 482:469–482.
1165 Wise SP, Murray EA (2000) Arbitrary associations between antecedents and actions.
1166 Trends Neurosci 23:271–276.
1167 Yeo BT, Krienen FM, Chee MW, Buckner RL (2013). Estimates of segregation and
1168 overlap of functional connectivity networks in the human cerebral cortex.
1169 Neuroimage. 88C:212-227.
1170 Yin HH, Knowlton BJ (2006) The role of the basal ganglia in habit formation. Nature
1171 Reviews Neurosci 7:464–476.
1172 Zalesky A, Fornito A, Cocchi L, Gollo LL, Breakspear M (2014). Time-resolved
1173 resting-state brain networks. Proc. Natl Acad. Sci. USA 111, 10341–10346.

# FIGURE and TABLE LEGENDS

**Figure 1**. (A) Arbitrary visuomotor mapping task. (B) *MarsAtlas*: cortical parcellation displaying the anatomical gradients both in the rostro-caudal and dorso-ventral directions; for a detailed description see Auzias and collaborators (2016). (C) *MarsAtlas:* single-subject exemplar volumetric representation displaying subcortical regions included in the atlas: nucleus accumbens, amygdala, hippocampus, globus pallidus, putamen, caudate nucleus and thalamus.

**Figure 2**. Statistical map displaying the brain areas associated with a significant increases in HGA with respect to baseline (time-point and cluster-level threshold were set to $q < 0.001$ FDR-corrected). The anatomical labels of subcortical areas are NAc (nucleus accumbens), Amyg (amygdala), Hipp (hippocampus), GP (globus pallidus), Put (putamen), Cd (caudate nucleus), Thal (thalamus).

**Figure 3**. Strength of the Functional Link (SFL). (A) Mean SFL connectivity matrix averaged over time. (B) SFL time course averaged over pairs of areas. The threshold for significant SFL was equal to 2.43. Error bars correspond to 95% confidence interval.

**Figure 4**. Graph theoretical measures. (A) Dependence between threshold values (q-values) and FC density. (B) Temporal evolution of density D at $q = 0.05$.

**Figure 5**. Functional Connectivity Dynamics (FCD). (A) Time course of the average SFL (Strength of Functional Link) for the three identified Link Communities (LC). Error bars correspond to 95% confidence interval. Spatial patterns for the three LCs are displayed in (B), (C) and (D). The thickness of the green links is proportional to the time-averaged SFL between areas, whereas the colour and size of nodes is proportional to the mean SFL between each area and the rest of the network (i.e., the weight).

**Figure 6**. Exemplar evolution for the dorsolateral motor (A, C) and premotor (B, D) areas. (A) and (B) show the involvement of MdI and PMdI in the three LCs, respectively. (C) and (D) depict the involvement in percentage value.

**Figure 7**. Flexibility analysis. (A) Mean evolution of network flexibility (shaded area represent standard deviation). (B) Areal flexibility for the five most representative brain regions.

**Figure 8**. Relation between mean FC and distance for the thalamus (A) and caudate nucleus (B). Each dot corresponds to a brain area displaying significant FC with the seed regions.

**Figure 9.** Distribution of normalized inner products between the average dipole orientations of the left thalamus and caudate nucleus across participants (A). The boxplot depicts extreme values (whiskers), first and third quartile (box) and median (red line). (B) Time course of mean correlation coefficient.

**Figure 10**. SEEG validation of HGA modulations. Comparison between SEEG single-subjects t-value for HGA (blue) and group-level MEG results (red curves). Subject number, brain areas and the correlation coefficient between the curves is indicated on the top of each panel.

**Table 1.** Graph theoretical measures.

**Table 2.** SEEG activations

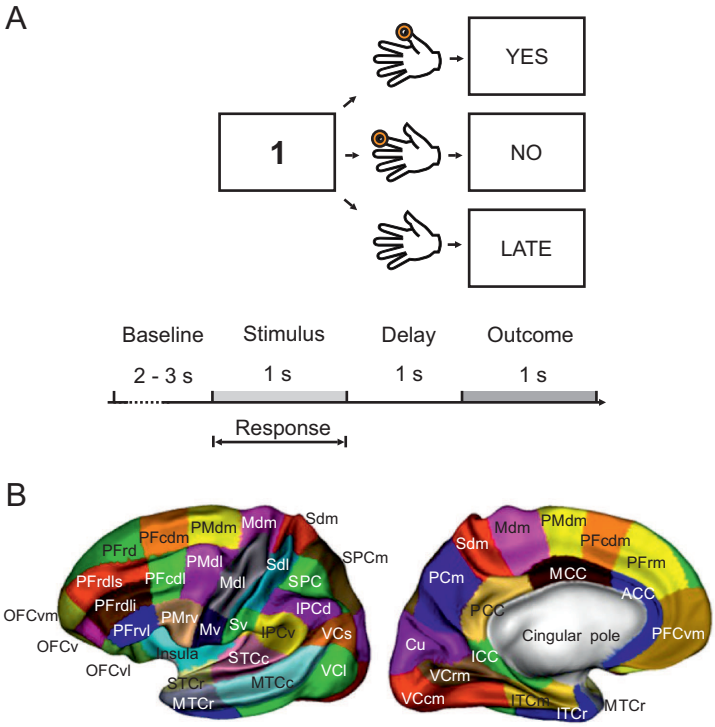

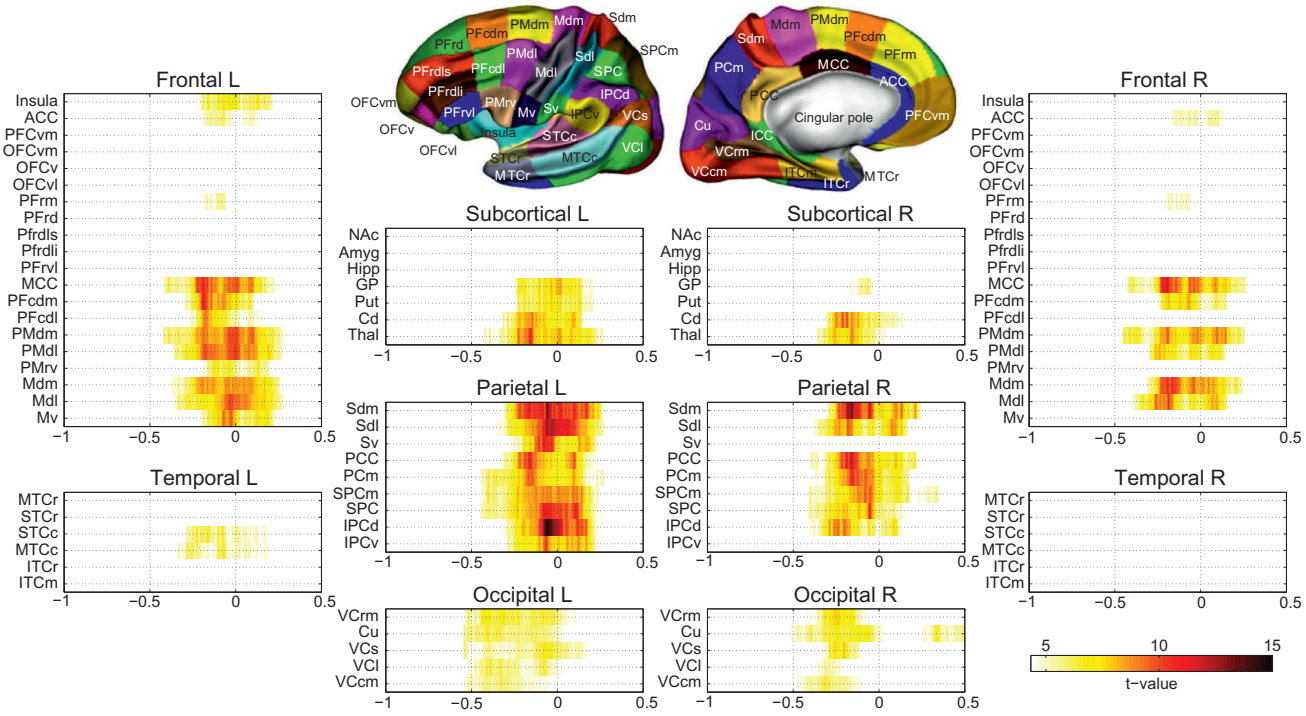

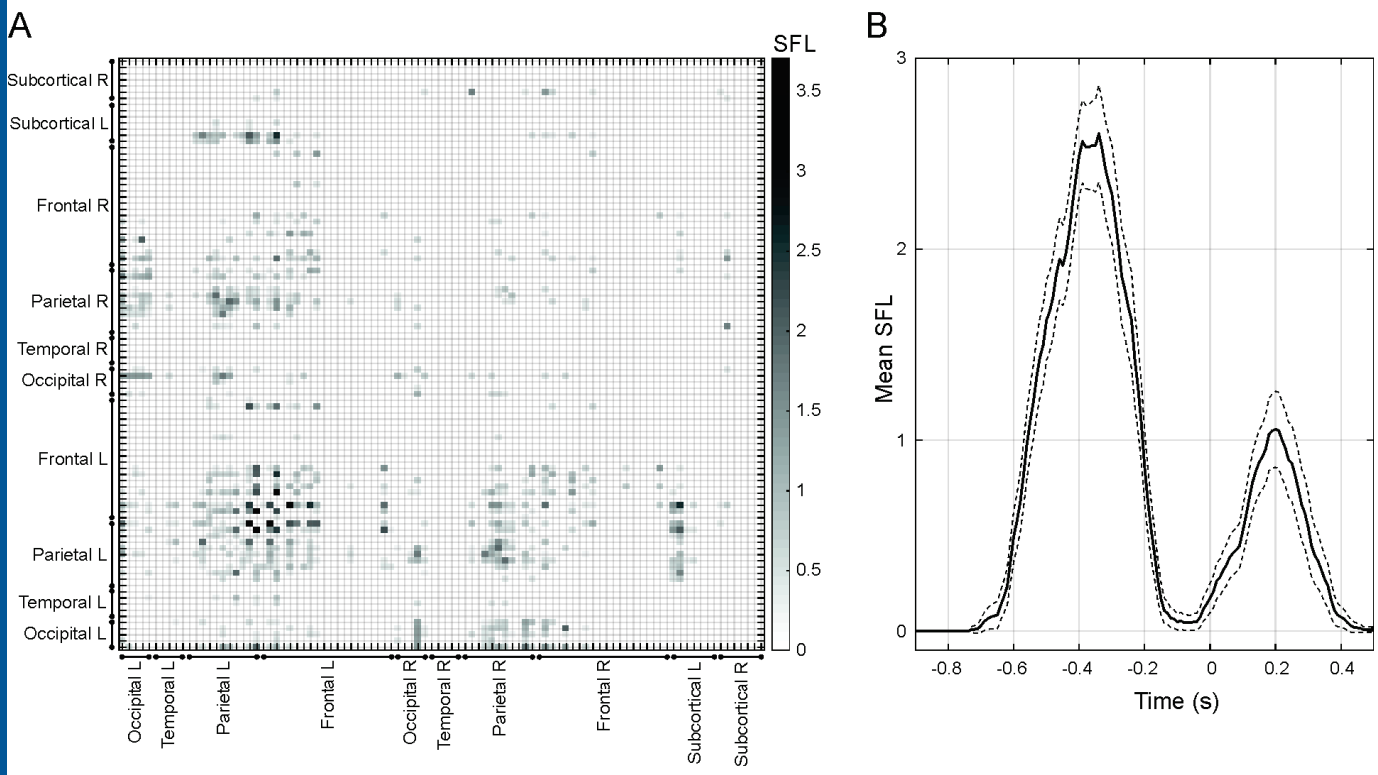

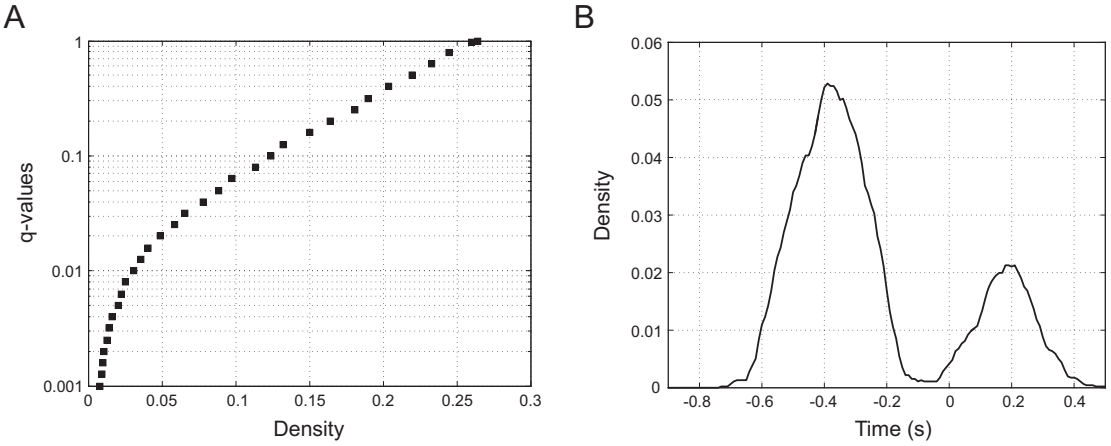

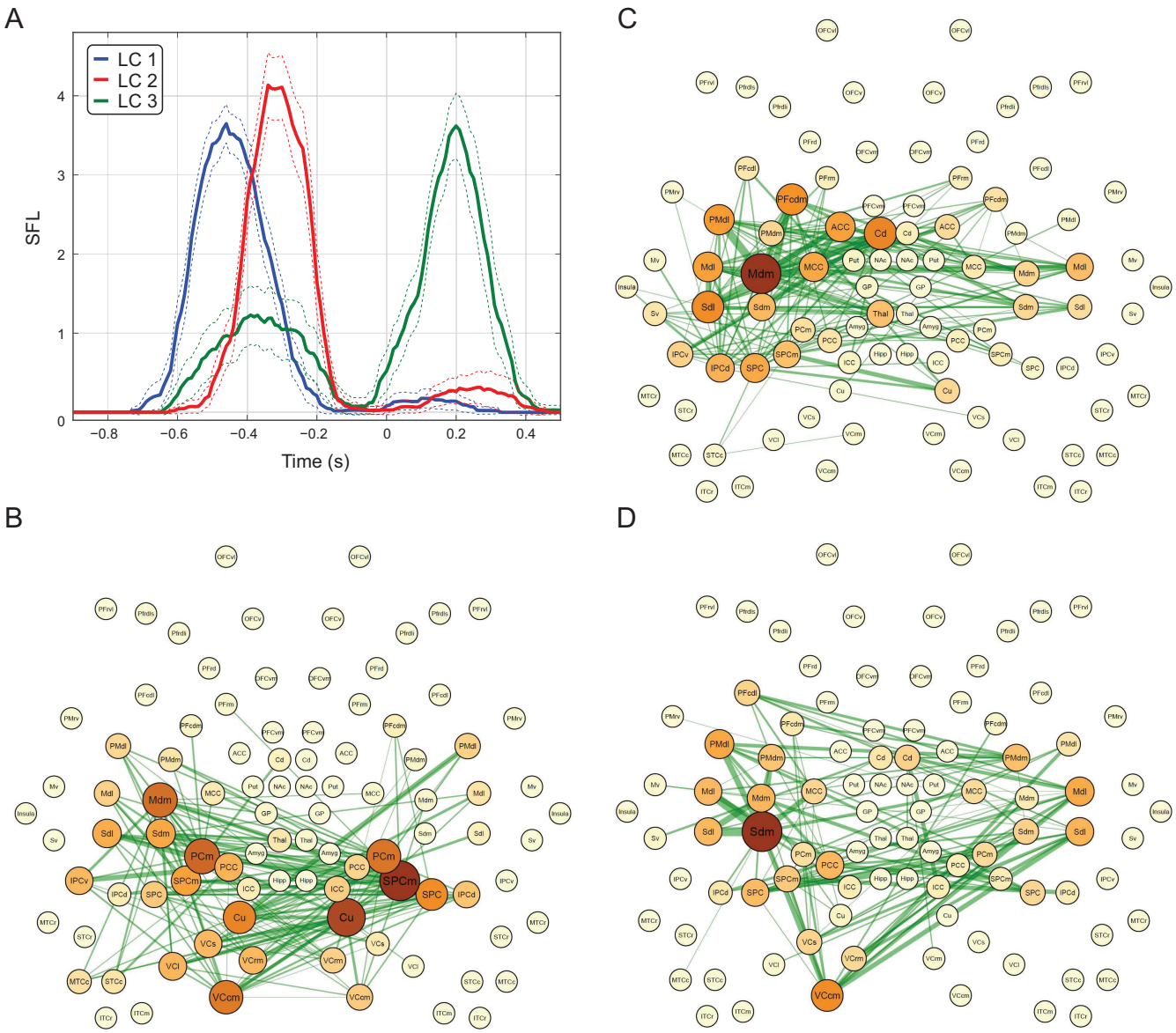

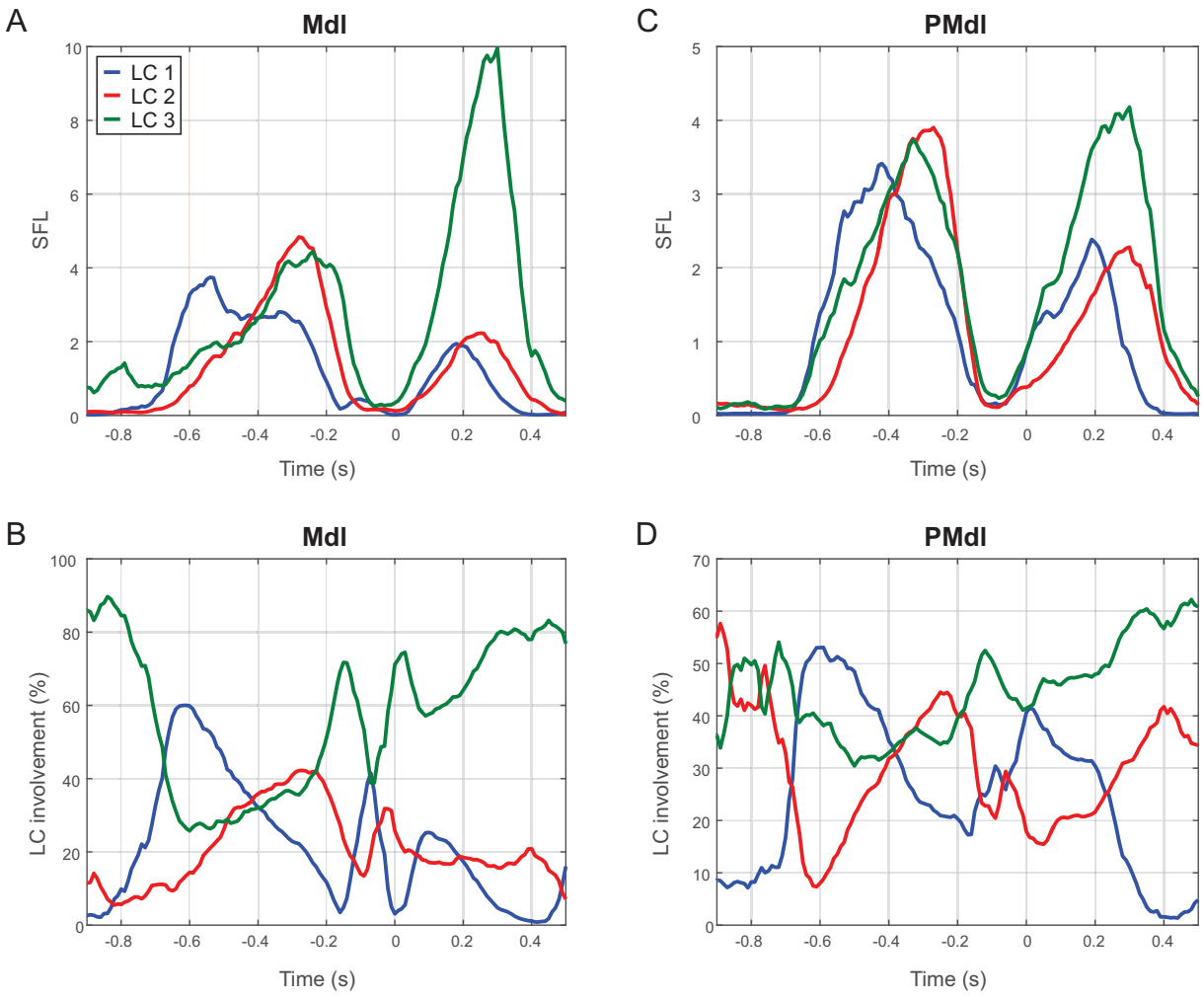

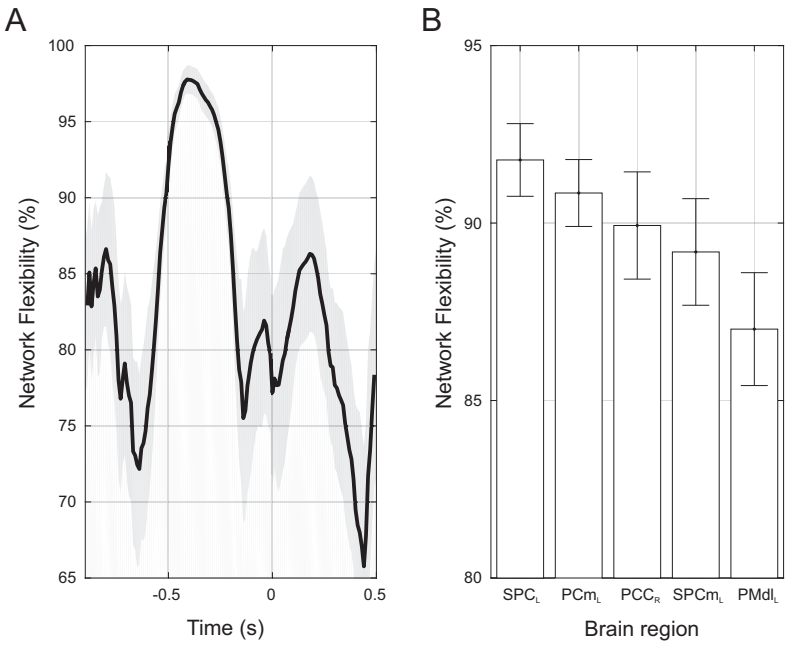

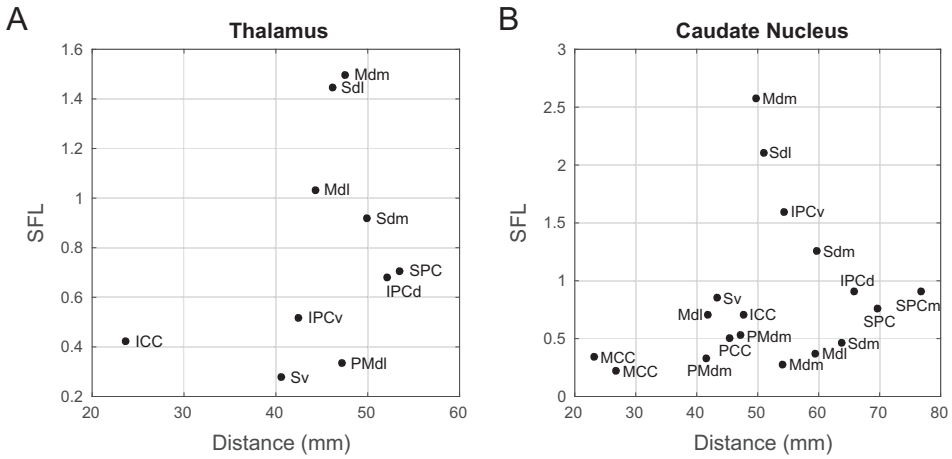

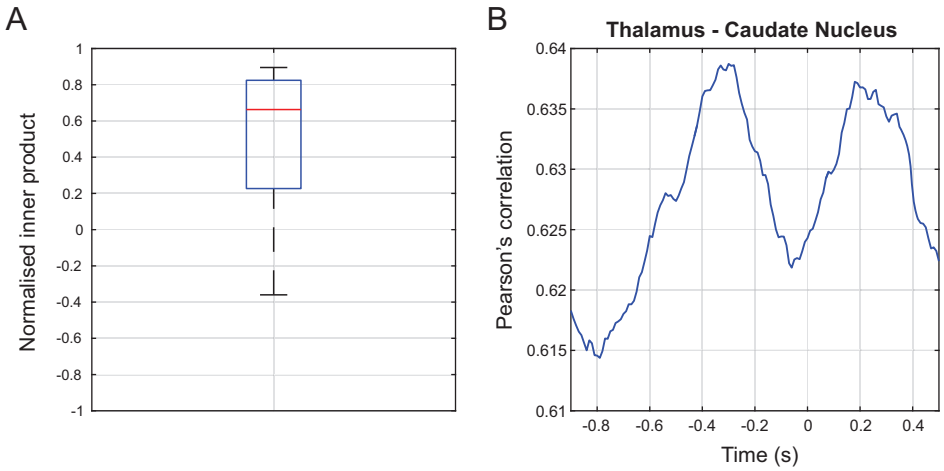

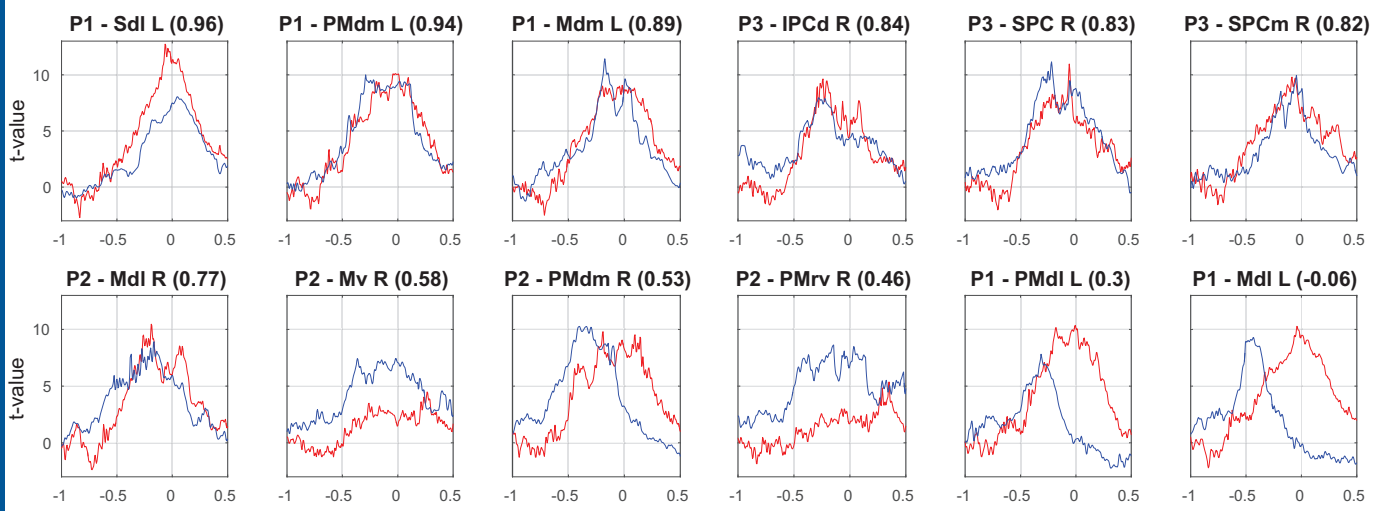

| Strength (S) | | Eigen Centrality (EC) | | Betweeness Centrality (BC) | |
|---|---|---|---|---|---|
| *Value* | *Region* | *Value* | *Region* | *Value* | *Region* |
| 7,39 | Mdm | 6,84 | Mdm | 16,25 | Sdm |
| 6,28 | Sdm | 6,42 | Sdm | 13,68 | Mdm |
| 4,64 | Sdl | 5,73 | Sdl | 9,98 | Cu |
| 3,88 | PMdl | 4,98 | Mdl | 9,52 | VCcm |
| 3,75 | VCcm | 4,37 | PMdl | 6,19 | Sdl |
| 3,70 | Mdl | 3,82 | Cd | 5,81 | Mdl |
| 3,34 | SPC | 3,56 | VCcm | 4,80 | PMdl |
| 3,25 | SPCm | 3,37 | SPCm | 4,46 | IPCd |
| 3,20 | Cu | 3,20 | PFcdm | 3,83 | SPC |
| 3,13 | Cd | 3,05 | PCC | 3,41 | SPCm |

| Parcel name | Peak *p-value* | Peak *t-value* | Peak time (s) | Time interval (s) | | Patient number |
|---|---|---|---|---|---|---|
| L Mdm | 3,42E-20 | 11,43 | -0,175 | -0,28 | 0,125 | 1 |
| R SPC | 8,76E-20 | 11,15 | -0,22 | -0,44 | 0,2 | 3 |
| R PMdm | 1,41E-17 | 10,27 | -0,34 | -0,62 | -0,06 | 2 |
| L PMdm | 5,65E-17 | 10 | -0,29 | -0,455 | 0,155 | 1 |
| R SPCm | 4,85E-17 | 9,96 | -0,045 | -0,275 | 0,05 | 3 |
| L Mdl | 2,21E-15 | 9,29 | -0,435 | -0,555 | -0,315 | 1 |
| R Mdl | 1,52E-14 | 8,92 | -0,165 | -0,39 | 0,055 | 2 |
| R PMrv | 6,70E-14 | 8,63 | -0,145 | -0,5 | 0,155 | 2 |
| L Sdl | 1,29E-12 | 8,05 | 0,045 | -0,225 | 0,26 | 1 |
| R IPCd | 1,69E-12 | 7,96 | -0,28 | -0,415 | -0,135 | 3 |
| L PMdl | 4,22E-12 | 7,82 | -0,315 | -0,45 | -0,185 | 1 |
| R Mv | 2,78E-11 | 7,44 | -0,02 | -0,44 | 0,18 | 2 |
| R Mdl | 9,89E-08 | 5,72 | -0,475 | -0,51 | -0,4 | 2 |